THE EFFECTS OF COMPRESSIBILITY ON THE PROPAGATION OF PREMIXED DEFLAGRATION

A Thesis Submitted to

the Faculty of Graduate and Postdoctoral Studies

by

Andre Fecteau, B.A.Sc

In Partial Fulfillment of the Requirements for the Degree of

MASTERS OF APPLIED SCIENCE

in Mechanical Engineering

Department of Mechanical Engineering

University of Ottawa

© Andre Fecteau, Ottawa, Canada, 2019

Acknowledgements

It is my pleasure to thank those who made this thesis possible, primarily to my supervisors Dr. James M^{c}Donald for his dedication to the success of my thesis and his open door policy that was indispensable during the course of my research and Dr. Matei Radulescu for his expertise and knowledge that was essential for me to make quick progress in my thesis and his critical feedback that helped me get better results.

I would also like to thank many of my fellow graduate colleagues at the University of Ottawa for their wonderful collaboration, continuous support in accomplishing my research and for making my graduate degree experience memorable.

I would like to give a warm thanks to my family for supporting me through the writing on this thesis and my life in general. Last but not least, I am grateful for the support of my friends, we were not only able to support each other in deliberating over our problems and findings, but also happily by talking about things other than just our papers.

Abstract

The thesis addresses the influence of compressible effects on the stability of deflagration waves. Due to the quasi-isobaric nature of slow flames, compressible effects in laminar flames are usually neglected. Nevertheless, turbulent deflagrations may propagate at substantially higher speeds, suggesting that compressible effects may play a role in their dynamics. In the present thesis, the stability of diffusion-dominated high-speed deflagrations is addressed. The deflagration is studied in the thickened regime, hence addressing the long wavelength limit of these deflagrations. The deflagrations are modelled by the compressible reactive Navier-Stokes equations with a single-step Arrhenius reaction model. The 2D stability of the steady traveling-wave solution is studied by direct simulation. It is found that, as the flame compressibility becomes significant, not only does the growth rates of the cellular profile of the deflagration waves increase, but the traditional correlation of the burning velocity and the flame surface area become far less strong. Significant compression regions form in front of the nonlinear flames. These compression regions have been found to increase the growth rates by increasing the temperature of the unburned gas in front of the flames, as well as convecting the flame forward. The results show that the flame propagation velocity in references to the unburned gas was significantly faster than the burning velocity. The vorticity was given consideration, as the compressibility of flame increase one can expect the baroclinic source to be of greater significance. The vorticity was show to, in effect, increase as compressibility increases while unexpectedly having a stabilizing direction of rotation on the cellular structure of the flames.

Keywords: Deflagration Instability, Fast Flames, One-Step Chemistry, Vorticity.

Table of Contents

List of Tables

List of Figures

Chapter 1

Introduction

The process in which flames transition from deflagration to detonation (DDT) is not fully understood. Avoiding these transition in industrial disaster is extremely important, since over-pressures created by detonation waves can have disastrous consequences. Example of such a disaster are the 2005 Hertfordshire oil storage terminal fire [1] and the 1970 propane vapour cloud explosion in Port Hudson [2]. The current level of understanding of deflagration to detonation transition is summarized by Ciccarelli and Dorofeev [3] and Oran and Gamezo [4]. The transition problem corresponds to a change in fundamental propagation mechanism, from diffusion dominated ignition mechanism to a gas dynamic auto-ignition dominated transport. Very recent developments have suggested that a sufficient criterion for DDT is the turbulent velocity reaching the Chapman-Jouguet (CJ) value, signifying that the burned gases reaches the sonic velocity in the flame frame of reference [5, 6]. At these speeds, compressibility effects are expected to play an important role. The development of a significant pressure wave increasing the temperature in front of the flames suggests that the propagation mechanism of such fast flames is not only via turbulent transport, but auto-ignition phenomena may begin to play a role. The present work focuses on clarifying the dynamics of diffusively controlled fast flame, where compressible effects may start influencing the dynamics.

Turbulent flames generate a pressure wave propagating ahead of the flame, the intensity of the pressure wave varies depending on the propagation velocity of the flame [7, 5]. Figure 1.1(a) shows a turbulent flame propagating to the right with a precompression region ahead of the reaction region. Experimental flames can be seen to be susceptible to the turbulence in the upstream flow. The different scales of turbulence modify the propagation of these flames in different ways. The smaller scales, or scales on the order of the flame thickness, increase the flame velocity by

(A) Experimental turbulent flame[8]. (B) Thickened reaction region.

FIGURE 1.1. Experimental turbulent flame and "Thickened-flame" representation

turbulent mixing of the burned and unburned gases. Larger scales on the other hand modify the general shape of the flame.

The Darrieus-Landau instability predicts the unconditional increase in the cellular structure of flames based purely on gas-dynamic arguments. One of the main goals of this thesis is to investigate to what degree this is true when some of the complexities of real flames are considered. The computational costs associated with fully resolving the smallest scales of a turbulent flow through a flame are prohibitive. In order make such a study more feasible, a thickened-flame approach is adopted that models the effects of small-scale turbulent structures on the flame. This thickened flame structure, illustrated in Figure 1.2, has artificially increased reaction rate that is meant to model the effect of turbulent mixing. The larger scales of turbulence are neglected, no forcing terms for turbulence are included in the model. Figure 1.1(b) relates an approximate zone in which the proposed model is correlated in experimental flames using a thick orange line. These one-dimensional thickened flame profile are modeled

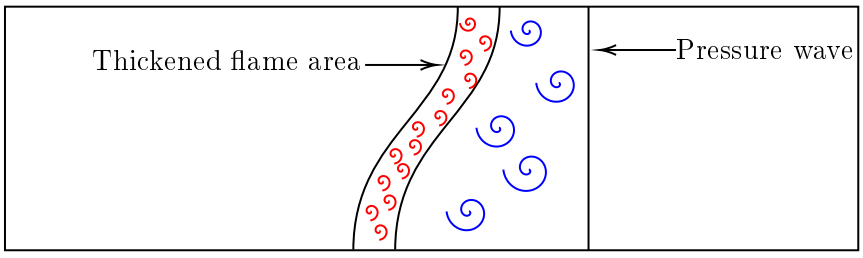

FIGURE 1.2. Comparitive turbulence length scales.

as laminar flames satisfying the Navier-Stokes equations, their reaction rate is modified to propagate at turbulent flame velocities. With the exception to the significant

pressure decrease through the flame, these one-dimensional profiles resemble flames in the laminar non-turbulent isobaric regime that numerous studies have analyzed [9, 10, 11, 12]. These flames are often assumed to travel with Mach numbers on the order of 10^{-3} and that the pressure in the flame is nearly constant through the flame. The effect of the Lewis number, Prandtl number, heat release of reaction and energy of activation on the propagation of these flames has been thoroughly studied previously. These studies have shown that incompressible flames travel in cellular structures with cusps-like structure between them. The growth rates of the cells are shown to be primarily dependent on the heat release of reaction, the energy of activation and the Lewis Number (Le). The effect of compressibility has been studied numerically in the linear regime by assuming that the flame can be represented as a laminar profile, as is done in this thesis, with a higher Arrhenius pre-exponential factor by [13, 12, 14, 15, 16] and briefly in the nonlinear regime [12]. It was found that the instability in compressible flames increases dramatically as they approach the CJ velocities. Bychkov [17] and He [18] have studied the stability of linear flames at the CJ velocity, their analysis shows that these flames are stable to all wavelengths. One of the goals of this thesis is to numerically verify the stability of these perturbed quasi-planar flame at the CJ velocities.

This thesis studies the evolution of two-dimensional flame profiles ranging from their quasi-isobaric velocities to their CJ deflagration velocity. The Navier-Stokes equations coupled with a single Arrhenius kinetic step is used. The initial conditions are chosen so as to minimize their effect on the initial growth rates of a laminar flame, a quasi-laminar extrapolation of the steady-state one-dimensional flame profile is used. An initial sinusoidal perturbation of the laminar profile is imposed so as to excite any instabilities.

It has often been shown that, in isobaric flames or even turbulent flames, the reaction rate is proportional to the surface area of the flame [19, 6]. This paradigm is tested for a range of flow velocities, where, in some flows, the compressibility is significant. The cellular instability of fast flames in the linear profile has also been shown to increase with respect to the flame velocity [13, 12]. This thesis extends the

evaluation of the growth rate of the cellular perturbation from the quasi-linear flame profile into non-linear configurations.

It has been theorized that vorticity induced by a compressible flame has a destabilizing effect [19]. One goal of this thesis is to quantify the relative importance of the different physical processes that are important for vorticity evolution near compressible flames. The overall importance of the resulting vorticity field on the flame stability is investigated for a range of flows. Vorticity has also been predicted to occur in the region between the concave and convex section of the flame [19], it is not inconceivable that the magnitude of vorticity depends on the amplitude of the cellular profile. Further analyses are done to quantify this ratio.

1.1 Structure of the Thesis

First, Chapter 2 explains the combustion process, including a literature review of the work that is relevant to the topics in this thesis. The problem of interest and relevant information as to why they were selected is shown in Chapter 3. The chosen model equations and non-dimesionalization scheme is explained in Section 3.1. This is followed by Chapter 4, in which possible methods for solving the one-dimensional flame profile are shown. The weaknesses and strengths of the Runge-Kutta 4 shooting method are analyzed in Section 4.1. Then, the derivation of the chosen implicit finite-volume method is shown in Section 4.2. Results of the one-dimensional solution are shown in Section 4.3 then validation of the numerical code and the one-dimensional resolution are done in Section 4.4. A review of a linear stability analysis of the linear isobaric deflagration is shown in Chapter 5. This linear stability analysis is useful for determining the wave number at which the flame instability is expected to appear in the two-dimensional simulations. The two-dimensional simulation is then presented in Chapter 6, starting with the explanation of the initial condition. Resolution and domain size choice are explained in Section 6.2. This is followed by a resolution study in Section 6.4 showing the effect of the cell resolution on the flame. Chapter 7 then analyses the results of the two-dimensional simulations. The results of the simulation are shown and explained as density profiles in Section 7.1. Section 7.2 analyses the

flame propagation velocity as a result of the cellular profile of the flames as well as the growth rates of these studied problems. Then, Section 7.3 discusses the identified potential causes for the increases of propagation and growth rates of compressible flames. Finally, Section 7.4 analyses the vorticity, its evolution, and its effect on the two-dimensional flames.

Chapter 2

Combustion Phenomena

For numerical modelling, it is convenient to categorize flames in a binary system of premixed and non-premixed combustion to root out fundamental processes of flames. In non-premixed combustion an interface separates the fuel and oxidizer, where, only through diffusion of species, can the combustion process occur. A premixed combustion defines a reaction happening in a medium where the oxidizer and fuel are already in a hydrodynamic equilibrium. In such a medium, species diffusivity and thermal diffusivity play an important role in the propagation of flames. While these categories are useful to gain insight into the underlying mechanisms of the combustion processes, often real-world practical applications utilize partially premixed flames. In this thesis, only premixed combustion is selected for study.

2.1 Flame Propagation in Premixed Medium

Premixed flames can propagate in two distinct modes, detonation or deflagration. A detonation is a compression wave and is supersonic, usually traveling on the order of kilometers per second. The structure of a detonation consists of the coupling of a shock and runaway thermal combustion following an ignition delay. This ignition delay is decreased by the increase of temperature induced by the shock, while the thermal runaway expansion of the gas sustains the shock. Experimentally detonation propagate at the Chapman-Jouguet (CJ) detonation velocity where the flow velocity behind the shock propagates at the speed of sound in the direction of the detonation or in a over-driven detonation where the velocity and pressure exceed the CJ criteria. The derivation for the CJ jump condition for ideal gases is shown in Section 3.3.

Deflagration is an expansion wave and propagates at subsonic velocities, usually on the order of meters per second. In this mode, convection and diffusion are the primary mode of propagation [20]. Unlike detonations, there is a range of velocities

at which deflagrations are stable, from the flame front propagating at very low speeds to the CJ deflagration velocity, where the Mach number of the burned flow is equal to unity. Within these flames, the pressure drops and the gas accelerates in the direction of the products of reaction. The size of the pressure drop in the flame depends on the burning velocity of the flame front, where slow moving flames are said to be isobaric. Fast flames can have a pressure drop of more than 50% in reference to the unburned gas.

Flames are intrinsically unstable and can propagate in non-planar fronts. In deflagration such deformation of the flame front modifies the unburned and burned gas by propagating pressure waves. In the unburned gas, these pressure waves can coalesce to form a significant pressure wave propagating in front of the flame. This means that the evolution of deflagration not only depends on the initial condition and the profile of the flame, but the perturbed fresh gas condition after these pressure waves [20].

2.2 Flame-Front Instabilities

It is well-known that, in experimental and numerical premixed flames, the flame front is rarely planar. The flame quickly forms a cellular structure with cusp-like sections between the cells, this region is indicated in the Figure 2.1. These instabilities in the flame front have the effects of increasing the flame velocity. A lot of research in the past has studied these instabilities in the flame front [23, 24, 26, 27, 9, 13, 10, 11], and three distinct modes have been identified as the primary modes of growth for the instabilities in isobaric flames: the Darrieus-Landau instability, the thermo-diffusive instability, and the instability caused by body forces. There are inherent difficulties when analyzing such disturbances in flames, the nonlinearity between the unburned perturbed flow and the three primary modes of instabilities complicate the investigation of any instability independently.

Under the isobaric, near-equidiffusional or respectively a Lewis number (Le) tending to unity ($Le \rightarrow 1$) and infinite activation energy ($E_a \rightarrow \infty$) approximation, Darrieus [23] and Landau [24] have predicted independently that, in a premixed com-

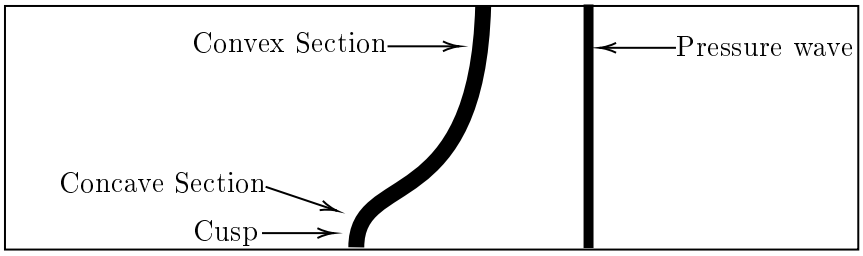

FIGURE 2.1. Flame configuration and naming convention

bustion, the cellular flame front would be unconditionally unstable with a growth rate proportional to the wave number as,

$$\bar{\sigma} = \bar{k}\bar{S}_L \frac{\Theta_2}{1+\Theta_2}\left(\left(1+\Theta_2-\frac{1}{\Theta_2}\right)^{1/2}-1\right), \tag{2.1}$$

where $\bar{\sigma}$ is the growth rate of the perturbances, $\Theta_2 = 1+Q$, $Q = \frac{\bar{Q}}{\bar{c}_p T_1}$ is the non-dimensional heat release of reaction, c_p is the specify heat capacity, $\bar{S}_L$ is the velocity of the flame and $\bar{k}$ is the wave number of the perturbation. Variables denoted with an overbar represent dimensional values, while, unless indicated otherwise, all other variables are expressed using the non-dimensionalization scheme shown in Section 3.1.4. Darrieus and Landau have shown that the flow profile created by curved flames create a converging-diverging nozzle effect in the concave-convex section of the flames in the unburned gas. Assuming that the velocity of the flame is not affected by its shape and propagates perpendicularly to the flame front, the concave section of the flame propagating in the unburned flow accelerate due to the flow being decelerated and the flame front in the convex section decelerates due to the flow acceleration [29]. This effect is visualized in Figure 2.2, where the thicker dark vertical line is the reaction zone and the horizontal lines are the stream lines. In this situation the unburned flow is incoming from the left and the flame is stationary. In Figure 2.2, it can be seen that the unburned streamlines diverge in the convex section of the flames, this indicates a flow that is decelerating. In the concave section of the flame, the streamlines are converging closer together, this indicates an acceleration of the flow.

Moreover, Clavin and Williams [26] and Peke and Clavin [27] accounted for the first-order correction to the isobaric flames from the effect of the flame thickness or

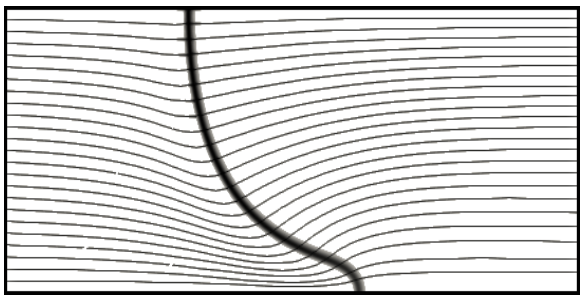

FIGURE 2.2. Stream lines in a deflagration flame.

thermal-diffusive ratios and showed that the flame thickness has a stabilizing effect. The thermo-diffusive instability is a competition between the stabilizing effect of mass diffusion and the destabilizing effects of thermal diffusion. The Lewis number (Le), defined as the ratio between the thermal diffusivity and the mass diffusivity, it is the non-dimensional number that embodies this effect. As one can see in Figure 2.3, if the thermal diffusivity (red arrows) is greater than the mass diffusivity (white arrows), the concave parts of the flame tend to accelerate due to the thermal convergence increasing the temperature of the flame. This has a stabilizing effect on the flame. Alternatively, when the Lewis number is smaller than one, this stabilizing effect is reduced due to the concentration of mass flux driving into the flame convex part increasing its velocity [29]. Even if these analyses have limitations, further analytical work [9, 13, 10, 11] and numerically studies [12, 10, 11, 14, 15, 16] have reaffirmed that the non-linear effect of flame stretching and concentration of heat flux have a stabilizing effect on the flame. These studies have also shown that a reduction of the Lewis number increases the instability and the sensitivity to the energy of activation and that the Prandtl number and ratio of specific heats does not have a significant effect on the flame stability.

The effect of compressibility on the instability of premixed flames have been studied analytically in the linear regime by Travnikov *et al.* [13]. They showed that, not only does the growth rate of a fast flame increase with the flame velocity, but the range of unstable wavelengths is also increased. Further numerical investigation by Travnikov *et al.* [12] confirmed the growth rates in the linear region that was found in their previous paper were correct. They also demonstrated that, in the

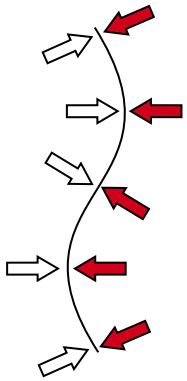

FIGURE 2.3. Thermo-diffusive instabilities in a deflagration flame.

compressible regime, the growth rate is affected by the precompression region in the unburned gases. Further analytical studies done by He [18] and Bychkov [17] have shown the instability in the linear domain rapidly disappears when approaching the CJ deflagration velocity.

To enhance the understanding of the effect of the compressibility on fast flames, this thesis systematically examines the effects of compressibility on the growth rate and propagation velocities of cellular flames by increasing the flame Mach number from the quasi-isobaric flame velocity to the CJ deflagration velocity. Body-force instabilities are due to external forces like gravity and electromagnetic fields. These effects are not considered in the chosen simulations, this is just to note that these forces can exert changes in the stability of the flames.

Chapter 3

Problem Definition

Recent experiments have shown that, prior to DDT, flames propagate at velocities close and above the CJ deflagration velocity [5]. In order to better understand these transitions, an understanding of the effects of compressibility in fast flames is important. In order to simulate the hydrodynamics of a deflagration flame, a thickened flame approach is utilized. This approach assumes that the flame acceleration from the effects of turbulence scales on the order and smaller than the flame thickness can be replaced by a laminar flame profile propagating at turbulent burning velocities. These laminar flame profile is assumed to satisfy the one-dimensional solutions to the Navier-Stokes equations. Turbulence scales larger than the flame thickness will be neglected. The non-equilibrium hydrodynamics of the system is chosen to be a one-step reaction model utilizing the Arrhenius equation.

Flame velocities from their quasi-isobaric to their CJ deflagration velocity are evaluated in a restricted domain width. The proposed reaction model is not representative of any specific real gas mixture due to its simplicity. These equations are, rather, a tool to investigate the effects of instabilities in flames and their sensitivity to macro-properties of reactions such as the energy of activation of a mixture and the heat release of reaction. In addition, fast flames are inherently turbulent, the model that is proposed uses laminar profiles with no turbulence model to simulate these flames. To achieve turbulent velocities using laminar flames, the pre-exponential factor of the Arrhenius reaction term can be increased. This increase in the rate constant of the reaction is analogous to the increase of diffusion due to turbulence and not a change in chemical kinetics [33]. A Lewis number of unity was also chosen to simulate that, in the fast-flame regime, where propagation is strongly affected by turbulence, one can expect reduced significance in the effect of the thermodiffusive instability. Travnikov *et al.* [13] have shown that the effect of γ and the Prandtl number did not affect the stability of the linear solution significantly. Travnikov *et al.* [13] have also

shown that the heat release of reaction and the energy of activation or the Zel'dovich number modified the instability of the cellular evolution of the flames. The four sets of numerical problems chosen for this study in this thesis are all possible combination of heat release $Q = 6, 9$ and Zel'dovich number $\beta = 5, 10$ where

$$\beta = \frac{QE_a}{(1+Q)^2}. \tag{3.1}$$

Here $Q = \frac{\bar{Q}}{\bar{c}_p \bar{T}_1}$ and $E_a = \frac{\bar{E}_a}{\bar{R}_g \bar{T}_1}$. The problems of interest in this thesis are summarized in Table 3.1.

TABLE 3.1. Problems of interest in the present work.

Name	γ	Pr	Le	Q	β
Problem 1	1.4	0.75	1	6	5
Problem 2	1.4	0.75	1	6	10
Problem 3	1.4	0.75	1	9	5
Problem 4	1.4	0.75	1	9	10

Varying the heat release of the reaction and the activation energy allows the effects of these parameters on compressible flows to be investigated independently. Each problem is then evaluated at different flame Mach numbers, ranging from the quasi-isobaric ($M_f = 0.03$) to their respective Chapman-Jouguet deflagration velocity (Problem 1 & 2: $M_f = 0.148777$) and (Problem 3 & 4: $M_f = 0.18028$). While increasing the Mach number of the flame, the significance of the pressure drop within the flame also increases. With these four problems, the effect of compressibility on the flame can be evaluated.

3.1 The Model

3.1.1 The Navier-Stokes Equations

In order to simulate the hydrodynamics of a deflagration flame, the compressible Navier-Stokes equations are used, coupled with a 1-step model to simulate the non-equilibrium hydrodynamics of the system. The governing equations are the conser-

vation of mass,

$$\frac{\partial \bar{\rho}}{\partial \bar{t}} + \frac{\partial \bar{\rho}\bar{u}_j}{\partial \bar{x}_j} = 0, \tag{3.2}$$

conservation of momentum,

$$\frac{\partial \bar{\rho}\bar{u}_i}{\partial \bar{t}} + \frac{\partial \bar{\rho}\bar{u}_i\bar{u}_j}{\partial \bar{x}_j} = -\frac{\partial \bar{p}}{\partial \bar{x}_i} + \frac{\partial \bar{\tau}_{ij}}{\partial \bar{x}_j} + \bar{f}_{2i}, \tag{3.3}$$

conservation of energy,

$$\frac{\partial \bar{\rho}\bar{e}}{\partial \bar{t}} + \frac{\partial \bar{\rho}\bar{u}_j\bar{e}}{\partial \bar{x}_j} + \frac{\partial \bar{p}\bar{u}_j}{\partial \bar{x}_j} = -\frac{\partial \bar{q''_{cj}}}{\partial \bar{x}_j} + \dot{\bar{q}''_g} + \frac{\partial(\bar{u}_k\bar{\tau}_{jk})}{\partial \bar{x}_j} + \vec{\bar{f}_{2j}} \cdot \bar{u_j}, \tag{3.4}$$

and species conservation,

$$\frac{\partial \bar{\rho}\bar{a}_i}{\partial \bar{t}} + \frac{\partial \bar{\rho}\bar{u}_j\bar{a}_i}{\partial \bar{x}_j} = \frac{\partial}{\partial \bar{x}_j}(\bar{\rho}\bar{\lambda}\frac{\partial \bar{a}_i}{\partial \bar{x}_j}) - \bar{\omega}_i \tag{3.5}$$

Here, $\bar{t}$ is the time, $\bar{x}_i$ is the position vector, $\bar{\rho}$ is the density, $\bar{u}_i$ is the flow velocity vector, $\bar{p}$ is the pressure, $\bar{\tau}_{ij}$ is the viscous stress tensor, $\bar{f}_{2j}$ is the body forces vector, $\bar{e}$ is the kinetic and thermal internal energy, $\bar{q_{cj}''}$ is the heat transfer by conduction and radiation, $\dot{\bar{q}''_g}$ is the heat generated by the exothermic reaction of the gas, $\bar{a}_i$ is the molar fraction of the i^{th} species, $\bar{\lambda}$ is the diffusion coefficient and ω_i is the rate of change of the concentration of the species i. Overbars denote dimensional properties, unless otherwise indicated.

3.1.2 Assumptions

The study presented in this thesis assumes that the gas follows the ideal gas law of the form $\bar{p} = \bar{\rho}\bar{R}_g\bar{T}$ where $\bar{R}_g$ is the specific gas constant and $\bar{T}$ is the temperature. The internal energy density of the gas is represented by $\bar{e} = \frac{1}{2}\bar{u}_i\bar{u}_i + \frac{1}{\gamma-1}\frac{\bar{p}}{\bar{\rho}}$, where γ is the ratio of the specific heats. The energy release is taken to be $\dot{\bar{q}''_g} = \bar{Q}_i\omega_i$, where $\bar{Q}_i$ is the heat release of the i^{th} reaction, the rate of reaction is taken in the form of the Arrhenius equation, $\omega_i = K_i\bar{\rho}\bar{a}_i e^{\frac{-(\bar{E}_a)_i}{\bar{R}\bar{T}}}$, where K_i is the pre-exponential factor and E_a is the activation energy, the body forces and radiation heat transfer is neglected, while the heat conduction is modelled using the Fourier Law $\bar{q''_{cj}} = -\bar{k}\frac{\partial \bar{T}}{\partial \bar{x}_j}$ and the viscous stress tensor has the form $\bar{\tau}_{ij} = \bar{\mu}((\frac{\partial \bar{u}_i}{\partial \bar{x}_j} + \frac{\partial \bar{u}_j}{\partial \bar{x}_i}) - \frac{2}{3}\delta_{ij}\frac{\partial \bar{u}_k}{\partial \bar{x}_k})$ where μ is the viscosity. Constant values through the combustion is assumed for the viscosity (μ), specify heat capacity ($\bar{c}_p$), thermal conductivity ($\bar{k}$) and diffusion coefficient ($\bar{\lambda}$).

3.1.3 The 1-Step Model

The simplest model for a chemical reaction involves a single step from reactants to products,

$$R \rightarrow P. \tag{3.6}$$

Using such an approximation allows one to define a progress variable, Y, such that Y is equal to the mass fraction of the reactants. For the present model, the rate of reaction is simplified by assuming it is only temperature dependent. This model neglects all intermediary steps in the reaction. Equations 3.2, 3.3, 3.4, 3.5 can then be simplified. The conservation of mass remains,

$$\frac{\partial \bar{\rho}}{\partial \bar{t}} + \frac{\partial \bar{\rho} \bar{u}_j}{\partial \bar{x}_j} = 0. \tag{3.7}$$

The conservation of momentum is now

$$\frac{\partial \bar{\rho} \bar{u}_i}{\partial \bar{t}} + \frac{\partial \bar{\rho} \bar{u}_i \bar{u}_j}{\partial \bar{x}_j} = -\frac{\partial \bar{p}}{\partial \bar{x}_i} + \frac{\partial \bar{\tau}_{ij}}{\partial \bar{x}_j}. \tag{3.8}$$

The conservation of energy is

$$\frac{\partial \bar{\rho} \bar{e}}{\partial \bar{t}} + \frac{\partial \bar{\rho} \bar{u}_i \bar{e}}{\partial \bar{x}_i} + \frac{\partial \bar{p} \bar{u}_i}{\partial \bar{x}_i} = \bar{k} \frac{\partial^2 \bar{T}}{\partial \bar{x}_i^2} + \frac{\partial \bar{u}_j \bar{\tau}_{ij}}{\partial \bar{x}_i} + \bar{Q} K \bar{\rho} \bar{Y} e^{\frac{-\bar{E}_a}{\bar{R}\bar{T}}}. \tag{3.9}$$

Finally, the species transport becomes,

$$\frac{\partial \bar{\rho} \bar{Y}}{\partial \bar{t}} + \frac{\partial \bar{\rho} \bar{u}_i \bar{Y}}{\partial \bar{x}_i} = \frac{\partial}{\partial \bar{x}_i} (\bar{\rho} \bar{\lambda} \frac{\partial \bar{Y}}{\partial \bar{x}_i}) - K \bar{\rho} \bar{Y} e^{\frac{-\bar{E}_a}{\bar{R}\bar{T}}}. \tag{3.10}$$

3.1.4 The Non-Dimensional Model

Extracting global relationships and tendencies from complex laws in often easier when they are presented in non-dimensional form. To make comparisons with previous works easier, the same non-dimensionalization used by Sharpe and Falle [11] is selected in this work. The non-dimensionalized equations are:

the conservation of mass,

$$\frac{\partial \rho}{\partial t} + \frac{\partial \rho u_j}{\partial x_j} = 0, \tag{3.11}$$

conservation of momentum,

$$\frac{\partial \rho u_i}{\partial t} + \frac{\partial \rho u_i u_j}{\partial x_j} = -\frac{\partial p}{\partial x_i} + \frac{\partial \tau_{ij}}{\partial x_j}, \tag{3.12}$$

conservation of energy,

$$\frac{\partial \rho e}{\partial t} + \frac{\partial \rho u_j e}{\partial x_j} + \frac{\partial p u_j}{\partial x_j} = \frac{\gamma}{\gamma - 1}\frac{\partial^2 T}{\partial x_j \partial x_j} + \frac{\partial u_j \tau_{ij}}{\partial x_i} + \hat{Q}W, \tag{3.13}$$

and species transport,

$$\frac{\partial \rho Y}{\partial t} + \frac{\partial \rho u_j Y}{\partial x_j} = \frac{1}{Le}\frac{\partial^2 Y}{\partial x_j \partial x_j} - W. \tag{3.14}$$

Here, the non-dimensional stress tensor is given by $\tau_{ij} = Pr\left(\frac{\partial u_i}{\partial x_j} + \frac{\partial u_j}{\partial x_i} - \frac{2}{3}\delta_{ij}\frac{\partial u_k}{\partial x_k}\right)$ and the reaction rate is $W = \Lambda \rho Y e^{-\hat{E}_a/T}$. Variable denoted by a subscript 1 and 2 are chosen to be the unburned and burned condition respectively. The non-dimensional variables are scaled using the following scheme:

$$x_i = \frac{\bar{\rho}_1 \bar{u}_1 \bar{c}_p \bar{x}_i}{\bar{k}}, \quad t = \frac{\bar{\rho}_1 \bar{u}_1^2 \bar{c}_p \bar{t}}{\bar{k}}, \quad u_i = \frac{\bar{u}_i}{\bar{u}_1}, \quad \rho = \frac{\bar{\rho}}{\bar{\rho}_1}, \quad e = \frac{\bar{e}}{\bar{u}_1^2},$$
$$p = \frac{\bar{p}}{\bar{\rho}\bar{u}_1^2}, \quad T = \frac{\bar{R}_g \bar{T}}{\bar{u}_1^2}, \quad \mathrm{Pr} = \frac{\bar{\mu}\bar{c}_p}{\bar{k}}, \quad \mathrm{Le} = \frac{\bar{k}}{\rho \bar{c}_p \bar{\lambda}}, \quad \Lambda = \frac{\bar{k}\bar{\Lambda}}{\bar{\rho}_1 \bar{u}_1^2 \bar{c}_p},$$
$$\hat{E}_a = \frac{E_a}{\gamma M_1^2}, \quad \hat{Q} = \frac{Q}{(\gamma - 1)M_1^2}, \quad Y = \frac{\bar{Y}}{\bar{Y}_1}.$$

Now that the non-dimensional scheme has been chosen, it is important to point out a few of the intrinsic effects of this scheme on the simulations. The first is that the space domain has been non-dimensionalized using the approximate length of the flame derived from the asymptotic treatment of the isobaric flame [42] ($\delta \approx \frac{\bar{k}}{\bar{\rho}_1 \bar{u}_1 \bar{c}_p}$) and that the time domain is now relative to τ_1, the time it takes the fluid to cross the flame. This means that, while comparing any properties that have a time or space unit, one has to realize that they are correlated with these new timescales and spacescales, relative to their flame Mach number.

3.1.5 Isobaric Equations

When flames propagate at very low velocities, they are often assumed to be isobaric. With this assumption, a simplified model can be developed from Equation 3.11–3.14.

The isobaric relation can be derived from the equation of state for pressure, $p = \rho T$, where p is assumed to be constant. This means that, throughout the domain, the density is inversely proportional to the temperature. A new, specific non-dimensional scheme for the isobaric equation can be derived with this relation in mind. The governing equations can be simplified, as shown by Sharpe [10]. Again, the continuity equation remains

$$\frac{\partial \rho}{\partial t} + \frac{\partial \rho u_j}{\partial x_j} = 0, \tag{3.15}$$

the conservation of momentum is,

$$\frac{\partial \rho u_i}{\partial t} + \frac{\partial \rho u_i u_j}{\partial x_j} + \frac{\partial P}{\partial x_i} = +\frac{\partial \tau_{ij}}{\partial x_j}, \tag{3.16}$$

the conservation of energy is,

$$\rho \frac{\partial \hat{T}}{\partial t} + \rho u_i \frac{\partial \hat{T}}{\partial x_i} = \frac{\partial^2 \hat{T}}{\partial x_i \partial x_i} + QW, \tag{3.17}$$

and the species transport is,

$$\frac{\partial \rho Y}{\partial t} + \frac{\partial \rho u_j Y}{\partial x_j} = \frac{1}{Le} \frac{\partial^2 Y}{\partial x_j \partial x_j} - W. \tag{3.18}$$

Here, the viscous terms in the energy equations and the pressure terms in Equation 3.12 are on the order of $\mathcal{O}(M_1^2)$ and are neglected. The pressure term P is the deviation of the pressure from the upstream pressure value. The non-dimensional stress tensor is given by $\tau_{ij} = Pr\left(\frac{\partial u_i}{\partial x_j} + \frac{\partial u_j}{\partial x_i} - \frac{2}{3}\delta_{ij}\frac{\partial u_k}{\partial x_k}\right)$ and the reaction rate is $W = \Lambda \rho Y e^{-E_a/T}$. The non-dimensional variables in this setting are scaled using the following scheme:

$$x_i = \frac{\bar{\rho}_1 \bar{u}_1 \bar{c}_p \bar{x}_i}{\bar{k}}, \quad t = \frac{\bar{\rho}_1 \bar{u}_1^2 \bar{c}_p \bar{t}}{\bar{k}}, \quad u_i = \frac{\bar{u}_i}{\bar{u}_1}, \quad \rho = \frac{\bar{\rho}}{\bar{\rho}_1}, \quad \hat{T} = \frac{\bar{T}}{T_1}, \quad \mathrm{Pr} = \frac{\bar{\mu}\bar{c}_p}{\bar{k}},$$
$$\mathrm{Le} = \frac{\bar{k}}{\rho \bar{c}_p \bar{\lambda}}, \quad \Lambda = \frac{\bar{k}\bar{\Lambda}}{\bar{\rho}_1 \bar{u}_1^2 \bar{c}_p}, \quad E_a = \frac{\bar{E}_a}{R_g T_1}, \quad Q = \frac{\bar{Q}}{c_p T_1}, \quad Y = \frac{\bar{Y}}{Y_1}, \quad \rho T = 1.$$

3.2 Steady-State Compressible Solution and One-Dimensional Burning Velocity

The unsteady multi-dimension system of equations presented in Section 3.1.4 can be simplified with the one-dimensional steady-state assumption, this means that all

time dependent derivatives are zero, the conservation of mass reduces to $u = \frac{1}{\rho}$. The governing equations are reduced to the conservation of linear momentum

$$\frac{\mathrm{d}u}{dx} = -\frac{\mathrm{d}p}{\mathrm{d}x} + \frac{\mathrm{d}\tau_{ij}}{\mathrm{d}x}, \tag{3.19}$$

the conservation of energy,

$$\frac{\mathrm{d}e}{\mathrm{d}x} + \frac{\mathrm{d}pu}{\mathrm{d}x} = \frac{\gamma}{\gamma - 1}\frac{\mathrm{d}^2T}{\mathrm{d}x^2} + \frac{\mathrm{d}u\tau_{ij}}{\mathrm{d}x} + \hat{Q}W, \tag{3.20}$$

and the species transport,

$$\frac{\mathrm{d}Y}{\mathrm{d}x} = \frac{1}{Le}\frac{\mathrm{d}^2Y}{\mathrm{d}x^2} - W. \tag{3.21}$$

Here, the non-dimensional stress tensor is given by $\tau_{ij} = Pr\left(\frac{4}{3}\frac{\mathrm{d}u_i}{\mathrm{d}x_j}\right)$ and the reaction rate is $W = \Lambda\rho Y e^{-\hat{E}_a/T}$. The non-dimensional variables are scaled using the following scheme:

$$x = \frac{\bar{\rho}_1\bar{u}_1\bar{c}_p\bar{x}}{\bar{k}}, \qquad u = \frac{\bar{u}}{\bar{u}_1}, \qquad \rho = \frac{\bar{\rho}}{\bar{\rho}_1}, \qquad e = \frac{\bar{e}}{\bar{u}_1^2},$$
$$p = \frac{\bar{p}}{\bar{\rho}\bar{u}_1^2}, \qquad T = \frac{\bar{R}_g\bar{T}}{\bar{u}_1^2}, \qquad \mathrm{Pr} = \frac{\bar{\mu}\bar{c}_p}{\bar{k}}, \qquad \mathrm{Le} = \frac{\bar{k}}{\rho\bar{c}_p\bar{\lambda}},$$
$$\Lambda = \frac{\bar{k}\bar{\Lambda}}{\bar{\rho}_1\bar{u}_1^2\bar{c}_p}, \qquad \hat{E}_a = \frac{E_a}{\gamma M_1^2}, \qquad \hat{Q} = \frac{Q}{(\gamma - 1)M_1^2}, \qquad Y = \frac{\bar{Y}}{Y_1}.$$

To fully constrain a set of three ODE's as shown above, three independent variables can be set. Also, for a steady-state solution to exist, the flame frame of reference must be chosen. Due to the non-dimensionalization chosen, one can fully constrain these equations by choosing the Mach number of the flame. Knowing the Mach number of the unburned flow and that the velocity and progress variable at the unburned conditions must be one, the pressure can be found using the Equation 3.22 and the temperature can be isolated from the equation of state for pressure.

$$M = \frac{u}{\sqrt{\gamma\frac{p}{\rho}}} \tag{3.22}$$

The CJ jump conditions shows that, for a fully constrained initial condition, there is only one possible jump condition through the flame. It was just shown that both the

upstream and downstream conditions are fully defined by choosing the Mach number of the flame. This also means that, between these two states, a constant rate of reaction of $\int_{-\infty}^{\infty} W \mathrm{d}x = 1$ must be exhibited across the flame since the reaction must burn all reactants across the flame.

3.3 Rankine-Hugoniot Flame Jump Conditions

The Rankine-Hugoniot jump conditions describe the flow conditions on either side of a discontinuity using the conservation of mass, momentum and energy across the discontinuity. These conditions lead to the relations

$$\frac{\bar{u}_1}{\bar{v}_1} = \frac{\bar{u}_2}{\bar{v}_2}, \tag{3.23}$$

$$\frac{\bar{u}_1^2}{\bar{v}_1} + \bar{p}_1 = \frac{\bar{u}_2^2}{\bar{v}_2} + \bar{p}_2, \tag{3.24}$$

$$\bar{h}_1 + \frac{1}{2}\bar{u}_1^2 + \bar{Q} = \bar{h}_2 + \frac{1}{2}\bar{u}_2^2. \tag{3.25}$$

Here, $\bar{v}$ is the specific volume.

3.3.1 Rayleigh Line

The Rayleigh line indicates the available states of pressure and specific volume through a discontinuity that conserves mass and momentum. One can obtain this relationship using Equation 3.23 and 3.24. The Rayleigh line is often represented as follows,

$$\frac{\bar{p}_2}{\bar{p}_1} = 1 + \frac{\bar{u}_1^2}{\bar{p}_1 \bar{v}_1}(1 - \frac{\bar{v}_2}{\bar{v}_1}). \tag{3.26}$$

3.3.2 Hugoniot Curve

The Hugoniot curve is similar to the Rayleigh line but instead is a curve that indicates the available states that conserve mass, momentum and energy across a discontinuity. Equation 3.23, 3.24, 3.25 and the thermodynamic relation $\bar{h} = \bar{e} + \bar{p}\bar{v}$ can be reduced to

$$\bar{e}_2 - \bar{e}_1 = \frac{1}{2}(\bar{p}_1 + \bar{p}_2)(\bar{v}_1 - \bar{v}_2) + \bar{Q}. \tag{3.27}$$

3.3.3 Rayleigh-Hugoniot plot

Figure 3.1 plots the Rayleigh line and Hugoniot curve on a plot of specific volume versus pressure. The Hugoniot curve is plotted on the plot in its entirety, while the Rayleigh line can change angle depending on the states chosen. The points of interest have been pointed out on the diagram, in both the deflagration and detonation domains, there are two solution for a given unburned flow velocity, except for the special case where the Rayleigh line is tangent to the Hugoniot curve. These intersections are commonly called the Chapman-Jouguet (CJ) conditions. These points occur in the fastest possible velocity for deflagration while in detonation this is the slowest possible velocity. The burned flow velocity at each CJ points is the speed of sound.

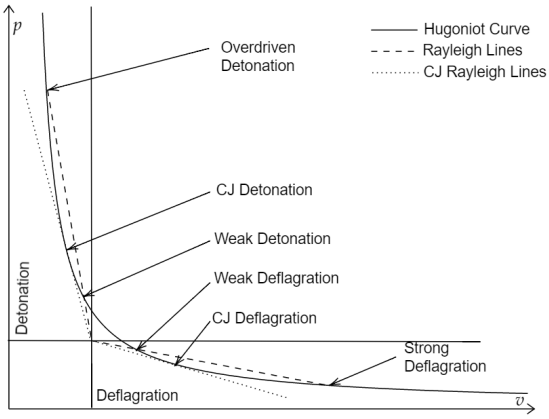

FIGURE 3.1. Hugoniot-Rayleigh curve

3.3.4 Flame Jump Conditions

Using the polytropic gas equation of state, $\bar{e} = \bar{c}_v \bar{T} = \frac{1}{\bar{\gamma}-1}\frac{\bar{p}}{\bar{\rho}}$, $\bar{c}^2 = \bar{\gamma}\frac{\bar{p}}{\bar{\rho}}$, and the Hugoniot curve, Equation 3.27, the final relation for the jump across a flame can be found,

$$(\frac{\bar{p}_2}{\bar{p}_1} + \frac{\bar{\gamma}-1}{\bar{\gamma}+1})(\frac{\bar{v}_2}{\bar{v}_1} - \frac{\bar{\gamma}-1}{\bar{\gamma}+1}) = 1 - (\frac{\bar{\gamma}-1}{\bar{\gamma}+1})^2 + \frac{2\bar{Q}}{\bar{p}_1\bar{v}_1}\frac{\bar{\gamma}-1}{\bar{\gamma}+1}.$$

Equation 3.26 can then be utilized to replace the pressure terms in the equations giving,

$$\frac{\bar{v}_2}{\bar{v}_1} = \frac{1+\bar{M}_1^2\bar{\gamma}}{\bar{M}_1^2(1+\bar{\gamma})} \pm \sqrt{\bar{\zeta}}, \tag{3.28}$$

where

$$\bar{\zeta} = \frac{2\bar{M}_1^2\bar{Q} + (-1+\bar{M}_1^2)^2\bar{p}_1\bar{v}_1\bar{\gamma} - 2\bar{M}_1^2\bar{Q}\bar{\gamma}^2}{\bar{p}_1\bar{v}_1(1+\bar{\gamma})^2\bar{M}_1^4\bar{\gamma}}.$$

The density jump condition is

$$\frac{\bar{v}_2}{\bar{v}_1} = \frac{1+M_1^2\gamma}{M_1^2(1+\gamma)} \pm \sqrt{\bar{\zeta}}, \tag{3.29}$$

the velocity jump condition is

$$\frac{\bar{u}_2}{\bar{u}_1} = \frac{1+M_1^2\gamma}{M_1^2(1+\gamma)} \pm \sqrt{\bar{\zeta}}, \tag{3.30}$$

and the pressure jump condition is

$$\frac{\bar{p}_2}{\bar{p}_1} = \frac{1+M_1^2\gamma}{(1+\gamma)} \pm \gamma M_1^2\sqrt{\bar{\zeta}}. \tag{3.31}$$

3.3.5 Determining the CJ Point

Analyzing the jump equations, one can see that $\sqrt{\zeta}$ must be positive. The point at which $\zeta = 0$ correspond to the CJ solution. We can determine the Mach number at which the CJ solution is found using,

$$M_1 = \sqrt{1 - \frac{\bar{Q}}{\bar{p}_1\bar{v}_1\gamma} + \frac{\bar{Q}\gamma}{\bar{p}_1\bar{v}_1} \pm \frac{\sqrt{\bar{Q}(-1+\gamma^2)(-\bar{Q}+2\bar{p}_1\bar{v}_1\gamma+\bar{Q}\gamma^2)}}{\bar{p}_1\bar{v}_1\gamma}}. \tag{3.32}$$

Chapter 4

Numerical Methods to Obtain One-Dimensional Steady-State Flame Structures

To be able to set adequate initial conditions for the proposed problems with two space dimensions, a one-dimension steady-state flame structure needs to be resolved. Unfortunately, for a given (Le, Pr, γ, Q, $\hat{T}$) the value of Λ needed to correspond to a flame with a desired Mach number cannot be easily found. Since the time-steps are limited by the stiffness of the second derivatives at the scales required to resolve the flame structure and that the flame structure must be solved by iteration to find the appropriate Λ in a reasonable time, a time efficient method must be used to solve these profiles. Traditionally, one-dimensional solutions have been found using a shooting method, but it was found that, when using the method described in Travnikov [13] that, for flow approaching the CJ velocity, the shooting method does not always converge to the correct solution through its temperature diffusion zone due to numerical errors. To handle this problem, a one-dimensional finite-volume solver with implicit time marching is used.

4.1 Compressible Shooting Method

Traditionally, shooting methods are used to find the steady one-dimensional solution to the set of equations describing isobaric flames[13]. Starting from the governing equations presented in Section 3.1.4, with the one-dimensional steady-state assumption, this means that all time dependent derivatives are zero, the conservation of mass reduces to $u = \frac{1}{\rho}$. The governing equations are reduced to,

$$\frac{4}{3} Pr \gamma M_1^2 \frac{\mathrm{d}U}{\mathrm{d}x} = \frac{\hat{T}}{U} - 1 + \gamma M_1^2 (U - 1), \tag{4.1}$$

$$\frac{\mathrm{d}\hat{T}}{\mathrm{d}x} + Le \frac{\mathrm{d}Y}{\mathrm{d}x} = \frac{\gamma - 1}{\gamma} (U - \hat{T} - \frac{\gamma M_1^2}{2} (U - 1)^2) + \hat{T} - 1 + Y - Y_1, \tag{4.2}$$

$$Le\frac{\mathrm{d}^2Y}{\mathrm{d}x^2} - \frac{\mathrm{d}Y}{\mathrm{d}x} - \Lambda\frac{Y}{U}e^{-E_a/\hat{T}} = 0, \tag{4.3}$$

Here the system of equation has been non-dimensionalized using,

$$x = \frac{\bar{\rho}_1\bar{u}_1\bar{c}_p\bar{x}}{\bar{k}}\,, \quad \hat{T} = \frac{\bar{T}}{\bar{T}_1}\,, \quad \Lambda = \frac{\bar{\Lambda}\delta}{\bar{u}_1}\,, \quad E_a = \frac{\bar{E}_a}{\bar{R}\bar{T}_1}\,, \quad Y = \frac{\bar{Q}\bar{a}}{\bar{c}_p\bar{T}_1}\,, \quad U = \frac{\bar{\rho}_1}{\bar{\rho}} = \frac{\bar{u}}{\bar{u}_1}.$$

The solution to these equations can be estimated by posing the boundary conditions at either end of the solution, then marching in space while estimating the derivative of the solution from the previous solution in space to advance the solution forward. The boundary conditions for both the upstream and downstream state are,

$$\begin{aligned}
&x \to -\infty\,, \quad U = 1\,, \quad \hat{T} = 1\,, \quad \frac{\mathrm{d}Y}{\mathrm{d}x} = 0\,, \quad Y = \frac{1}{2}M_1^2(\gamma-1)(U_2^2-1) + \hat{T}_2 - 1\,,\\
&x \to \infty\,, \quad U = U_2\,, \quad \hat{T} = \hat{T}_2\,, \quad \frac{\mathrm{d}Y}{\mathrm{d}x} = 0\,, \quad Y = 0\,.
\end{aligned}$$

Here, U and $\hat{T}$ are one in the upstream state due to the non-dimensional scheme while Y is determined by the conservation of energy equation. The values of U_2 and $\hat{T}_2$ are calculated from the Rankine-Hugoniot jump condition described in Section 3.3. The solution can be integrated in space using a fourth-order Runge-Kutta integration scheme,

$$\begin{aligned}
\varphi_i^{n+1} &= \varphi_i^n + \frac{1}{6}(k_{1i} + 2k_{2i} + 2k_{3i} + k_{4i}),\\
k_{1i} &= \Delta x \cdot f_i(x^n, \varphi_j^n),\\
k_{2i} &= \Delta x \cdot f_i(x^n + \frac{\Delta x}{2}, \varphi_j^n + \frac{k_1}{2}),\\
k_{3i} &= \Delta x \cdot f_i(x^n + \frac{\Delta x}{2}, \varphi_j^n + \frac{k_{2j}}{2}),\\
k_{4i} &= \Delta x \cdot f_i(x^n + \Delta x, \varphi_j^n + k_{3j}),
\end{aligned}$$

where φ_j is an column vector of the primitive variables and the first derivative of Y, $f(x^n, \varphi_j^n)$ is defined by isolating the derivative of Equation 4.1–4.3, doing so gives,

$$f(x, U, \hat{T}, Y, \frac{\mathrm{d}Y}{\mathrm{d}x}) = \begin{bmatrix} \frac{\frac{\hat{T}}{U} - 1 + \gamma M_1^2(U-1)}{\frac{4}{3}Pr\gamma M_1^2} \\ -Le\frac{\mathrm{d}Y}{\mathrm{d}x} + \frac{\gamma-1}{\gamma}(U - \hat{T} - \frac{\gamma M_1^2}{2}(U-1)^2) + \hat{T} - 1 + Y - Y_1 \\ \frac{\partial Y}{\partial x} + \Delta x\frac{\partial^2 Y}{\partial x^2} \\ \frac{1}{Le}(\frac{\mathrm{d}Y}{\mathrm{d}x} - \Lambda\frac{Y}{U}e^{-\epsilon\hat{T}_2/\hat{T}}) \end{bmatrix}.$$

Typically the boundary conditions using a shooting method on non-reactive discontinuities are initialized in the post disturbed state and the solution is integrated from downstream to upstream. In the reactive model proposed above an additional equation to the shooting method is added for the progress variable, and due to the solution of this equations tending to zero before the temperature and pressure diffusive zone are solved, appropriate boundary conditions for the burned state were not able to be set to get the correct evolution to the problem. Using the unburned state as the initial conditions is the only option. To initialize a reaction, a small perturbation of $\frac{\partial Y}{\partial x} = -10^{-8}$ is used in the numerical solver while the other derivatives are set to zero.

The Arrhenius pre-exponential factor is initially unknown for any given flame state (Le, Pr, γ, Q, Θ). The value of the Arrhenius pre-exponential factor that is consistent with a steady flame must be found iteratively. In this method, the Arrhenius pre-exponential factor is found to be below its correct value if the progress variable never reaches zero, while the values is above the correct value if the progress variable becomes negative. A convergence problem arises in fast flames when the compressibility of the flame creates a peak in the temperature profile. The temperature diffusion zone then becomes difficult to resolve correctly due to a minor errors in any previous steps and the error due to the iteration of the Arrhenius pre-exponential factor. These errors make the solution diverge from the correct path to the downstream state. Figure 4.1 shows the solutions to the shooting method that were attained using double precision in both the space discretization and Arrhenius pre-exponential factor before the solutions diverge to infinity. The solution was stopped during the shooting method if $\hat{T} > \hat{T}_2$ and $\hat{T}_{n+1} - \hat{T}_{n-1} < 0$ or $Y_{n+1} - Y_{n-1} > 0$. The solutions of this method are compared with the solution found using the in-house implicit solver described in Section 4.2. One can notice that, when the one-dimensional solution does not have a temperature overshoot, the solution for the shooting method tangents the implicit solution before the end of the solution. In the fast flame, when a temperature overshoot become significant, to solve the flame profile requires the shooting method to stay on the solution path for a longer period after the reaction is complete to resolve the temperature relaxation zone. In these flames one can notice that, after the flame

starts to reduce in temperature, the shooting method diverges from the solution path. Even when the resolution of Λ and the space discretization are correct to machine precision, this divergence from the solution cannot be avoided. Due to this problem, this technique is used to find an approximate solution to warm start the implicit solver, the solution was also matched with the Navier-Stokes solution marching backwards from the unburned side to get a almost continuous initial condition throughout the domain.

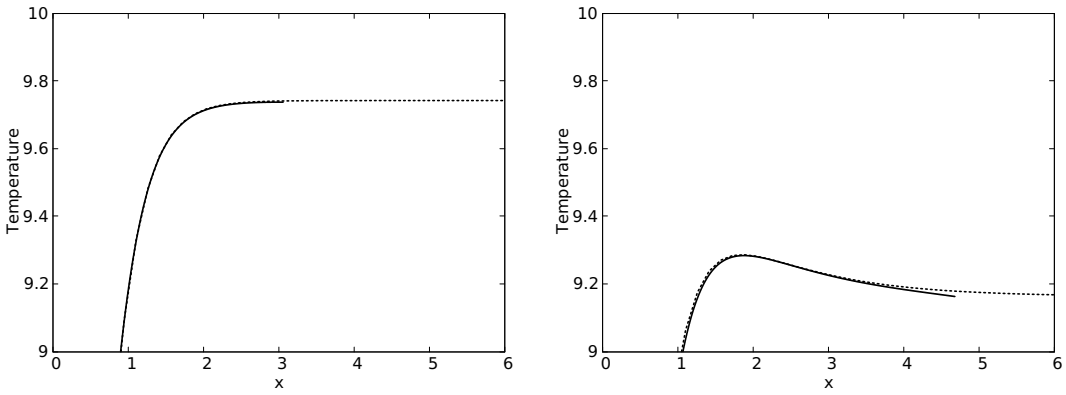

(A) $M_1 = 0.1$ (B) $M_1 = 0.14$

FIGURE 4.1. Shooting method solution for Problem 3: Shooting Method(——), Implicit Method (·····).

4.2 Implicit Numerical Scheme

As a traditional shooting method was found to be inadequate for the present study, an alternative method is needed. An implicit finite-volume scheme is chosen due to its stability at very large time-steps. Implicit methods are very useful when a steady-state solution is required, since the scheme is more diffusive in the transient domain but retains good accuracy when steady-state solution are converged. The scheme defined by Beam and Warming [22] is chosen for its flexibility to reproduce different schemes by changing run-time constants. The governing equations for the one-dimensional equations can be summarized using the form,

$$\frac{\partial U}{\partial t} + \frac{\partial F}{\partial x} = \frac{\partial V}{\partial x} + S, \tag{4.4}$$

where U, F,V and S for the set of equations proposed are defined by

$$U = \begin{bmatrix} \rho \\ \rho u \\ \rho e \\ \rho Y \end{bmatrix}, \qquad F = \begin{bmatrix} \rho u \\ \rho u^2 + p \\ \rho e u + p u \\ \rho Y u \end{bmatrix}, \qquad V = \begin{bmatrix} 0 \\ \tau_{xx} \\ \tau_{xx} u \\ \frac{1}{Le}\frac{\partial Y}{\partial x} \end{bmatrix}, \qquad S = \begin{bmatrix} 0 \\ 0 \\ QW \\ -W \end{bmatrix}.$$

The numerical scheme is posed as follows, where the notation was chosen as $\Delta\Phi^n = \Phi^{n+1} - \Phi^n$ where Φ is an arbitrary variable. In this section, a superscipt indicates the discrete time index, and a subscript indicates the index of a spatial cell.

$$\Delta U^n = \frac{\Theta \Delta t}{1+\epsilon}\left(\frac{\partial}{\partial t}\Delta U\right)^n + \frac{\Delta t}{1+\epsilon}\left(\frac{\partial}{\partial t} U\right)^n + \frac{\epsilon}{1+\epsilon}\Delta U^{n-1} + \mathcal{O}((\Theta - \frac{1}{2} - \epsilon)\Delta t^2 + \Delta t^3). \quad (4.5)$$

Where Θ and ϵ are constants used to determine the specific numerical scheme to be used. A first-order explicit Euler solver can be recovered by setting Θ and ϵ both to 0. If Θ is one, first-order implicit Euler can be recovered. A second-order time-accurate trapezoidal method can be found when Θ and ϵ are 0.5 and 0 respectively. Finally, the 3-point-backward method is recovered with $\Theta = 1$ and $\epsilon = 0.5$.

The time dependent derivatives can then be replaced in Equation 4.5 using the relation given in Equation 4.4,

$$\Delta U^n = \frac{\Theta \Delta t}{1+\epsilon}\frac{\partial}{\partial x}(\Delta F^n + \Delta V^n + \Delta S^n) + \frac{\Delta t}{1+\epsilon}\frac{\partial}{\partial x}(F^n + V^n + S^n) + \frac{\epsilon}{1+\epsilon}\Delta U^{n-1} + \mathcal{O}((\Theta - \frac{1}{2} - \epsilon)\Delta t^2 + \Delta t^3), \quad (4.6)$$

Using a Taylor series expansion, the fluxes can be linearized at time $n+1$ as,

$$\Delta F^n = A^n \Delta U^n + \mathcal{O}(\Delta t^2), \quad (4.7)$$

$$\Delta V^n = \left(P^n - \frac{\partial R^n}{\partial x}\right)\Delta U^n + \frac{\partial R^n \Delta U^n}{\partial x} + \mathcal{O}(\Delta t^2), \quad (4.8)$$

$$\Delta S^n = K^n \Delta U^n + \mathcal{O}(\Delta t^2), \quad (4.9)$$

where $A = \frac{\partial F}{\partial U}$, $P = \frac{\partial V}{\partial U}$, $R = \frac{\partial V}{\frac{\partial U}{\partial x}}$ and $K = \frac{\partial S}{\partial U}$ and $P - \frac{\partial R}{\partial x} = 0$, assuming constant fluid properties. These Jacobians have the form,

$$A = \begin{bmatrix} 0 & 1 & 0 & 0 \\ \frac{1}{2}(-3+\gamma)u^2 & (3-\gamma)u & -1+\gamma & 0 \\ -\frac{\gamma e u}{\rho} + (\gamma-1)u^3 & \frac{\gamma e}{\rho} - \frac{3}{2}(\gamma-1)u^2\gamma u^2 & \gamma u & 0 \\ -uY & Y & 0 & u \end{bmatrix},$$

$$R = \begin{bmatrix} 0 & 0 & 0 & 0 \\ -\frac{4\,\mathrm{Pr}\,u}{3\rho} & \frac{4\,\mathrm{Pr}}{3\rho} & 0 & 0 \\ \frac{(3\gamma-4\,\mathrm{Pr})\rho u^2-3\gamma e}{3\rho^2} & \frac{(4\,\mathrm{Pr}-3\gamma)u}{3\rho} & \frac{\gamma}{\rho} & 0 \\ -\frac{Y}{Le\rho} & 0 & 0 & \frac{1}{Le\rho} \end{bmatrix},$$

$$K = k_c \begin{bmatrix} 0 & 0 & 0 & 0 \\ 0 & 0 & 0 & 0 \\ Q\left(u^2 - \frac{e}{\rho}\right) & -Qu & Q & Q\frac{(\gamma-1)\left(\rho u^2-2e\right)^2}{4\Theta Y\rho^2} \\ -\left(u^2 - \frac{e}{\rho}\right) & u & -1 & -\frac{(\gamma-1)\left(\rho u^2-2e\right)^2}{4\Theta Y\rho^2} \end{bmatrix}.$$

Here, $k_c = \frac{4\lambda\Theta Y\rho^2 \exp\left(\frac{2\Theta\rho}{(\gamma-1)(\rho u^2-2e)}\right)}{(\gamma-1)(\rho u^2-2e)^2}$. Using the linearized relations 4.7, 4.8 and 4.9, Equation 4.6 becomes

$$I\Delta U^n + \frac{\Theta\Delta t}{1+\epsilon}\Big(- K^n\Delta U^n + \frac{\partial A^n\Delta U^n}{\partial x} - \frac{\partial^2 R^n\Delta U^n}{\partial x^2}\Big) = \frac{\Delta t}{1+\epsilon}\big[S^n + \frac{\partial}{\partial x}(-F^n + V^n)\big] + \frac{\epsilon}{1+\epsilon}\Delta U^{n-1} + \mathcal{O}(\big(\Theta - \frac{1}{2} - \epsilon\big)\Delta t^2, \Delta t^3). \quad (4.10)$$

Here, I is the identity tensor.

Choosing the space discretization with care, it is possible to limit the pre-ΔU^n left-hand side (LHS) matrix to be tridiagonal. Doing so will allow the utilization of the Taylor algorithm to accelerate the inversion of this matrix. The first step is to separate the derivatives using the product rule $\frac{\partial f(x)g(x)}{\partial x} = g(x)\frac{\partial f(x)}{\partial x} + f(x)\frac{\partial g(x)}{\partial x}$ and $\frac{\partial^2 f(x)g(x)}{\partial x^2} = g(x)\frac{\partial^2 f(x)}{\partial x^2} + \frac{\partial g(x)}{\partial x}\frac{\partial f(x)}{\partial x} + f(x)\frac{\partial^2 g(x)}{\partial x^2}$. This leads to

$$I\Delta U^n + \frac{\Theta\Delta t}{1+\epsilon}\left[\left(\frac{\partial A^n}{\partial x} - \frac{\partial^2 R^n}{\partial x^2} - K^n\right)\Delta U^n + \left(A^n - 2\frac{\partial R_n}{\partial x}\right)\frac{\partial\Delta U^n}{\partial x} - R^n\frac{\partial^2\Delta U^n}{\partial x^2}\right] = \frac{\Delta t}{1+\epsilon}\left[S^n + \frac{\partial}{\partial x}(-F^n + V^n)\right] + \frac{\epsilon}{1+\epsilon}\Delta U^{n-1} + \mathcal{O}(\big(\Theta - \frac{1}{2} - \epsilon\big)\Delta t^2, \Delta t^3). \quad (4.11)$$

The derivatives of A, R and K can be found algebraically, while $\frac{\partial\Delta U}{\partial x}$ is approximated using centered differences or the HLLE flux function, as discussed in the next section, and $\frac{\partial^2\Delta U}{\partial x^2}$ is evaluated using centered differences

Boundary conditions considered for this implicit scheme are the Dirichlet and zero gradients boundary conditions. The tridiagonal matrix multiplying ΔU on the left-hand side has the form,

$$\begin{bmatrix} 1+a_0 & b_0 & 0 & \vdots & 0 & 0 & 0 \\ c_1 & 1+a_1 & b_1 & \vdots & 0 & 0 & 0 \\ 0 & c_2 & 1+a_2 & \ddots & 0 & 0 & 0 \\ \dots & \dots & \ddots & \ddots & \ddots & \dots & \dots \\ 0 & 0 & 0 & \ddots & 1+a_{n-2} & b_{n-2} & 0 \\ 0 & 0 & 0 & \vdots & c_{n-1} & 1+a_{n-1} & b_{n-1} \\ 0 & 0 & 0 & \vdots & 0 & c_n & 1+a_n \end{bmatrix} \tag{4.12}$$

Dirichet boundary conditions do not affect the LHS matrix. The zero gradient boundary condition can be achieved by adding the values of c_0 and b_n to the first and last entry in the diagonal of the matrix as follows,

$$\begin{bmatrix} c_o+1+a_0 & b_0 & 0 & \vdots & 0 & 0 & 0 \\ c_1 & 1+a_1 & b_1 & \vdots & 0 & 0 & 0 \\ 0 & c_2 & 1+a_2 & \ddots & 0 & 0 & 0 \\ \dots & \dots & \ddots & \ddots & \ddots & \dots & \dots \\ 0 & 0 & 0 & \ddots & 1+a_{n-2} & b_{n-2} & 0 \\ 0 & 0 & 0 & \vdots & c_{n-1} & 1+a_{n-1} & b_{n-1} \\ 0 & 0 & 0 & \vdots & 0 & c_n & 1+a_n+b_n \end{bmatrix} \Delta U = \begin{bmatrix} RHS_1 \\ RHS_2 \\ RHS_3 \\ RHS_4 \\ \vdots \\ RHS_{n-2} \\ RHS_{n-1} \\ RHS_n \end{bmatrix},$$

Two different methods have been compared when calculating the first-order derivatives fluxes between the cells while keeping a second-order centered difference scheme. Second derivative are approximated using

$$\frac{\partial^2 \Phi}{\partial x^2} = \frac{\Phi_{i+1} - 2\Phi_i + \Phi_{i-1}}{2\Delta x^2}. \tag{4.13}$$

For the first derivatives, a centered-difference scheme with artificial dissipation, as described in Beam and Warming [22], as well as the HLLE flux calculator [28] are implemented. The components of the above matrix a_n, b_n and c_n can be separated as:

$$a_n(K, A, R) = a_n(A) + a_n(R) + a_n(K),$$

$$b_n(K,A,R) = b_n(A) + b_n(R) + b_n(K),$$
$$c_n(K,A,R) = c_n(A) + c_n(R) + c_n(K),$$

where,

$$a_n(R) = \frac{\Theta}{1+\zeta}\Delta t(-\frac{R_{n+1} - 2R_n + R_{n-1}}{\Delta x^2} + 2\frac{R_n}{\Delta x^2}),$$
$$b_n(R) = \frac{\Theta}{1+\zeta}\Delta t(-\frac{R_{n+1} - R_{n-1}}{\Delta x^2} - \frac{R_n}{\Delta x^2}),$$
$$c_n(R) = \frac{\Theta}{1+\zeta}\Delta t(\frac{R_{n+1} - R_{n-1}}{\Delta x^2} - \frac{R_n}{\Delta x^2}),$$

and,

$$a_n(K) = \frac{\Theta}{1+\zeta}\Delta t(-K),$$
$$b_n(K) = 0,$$
$$c_n(K) = 0.$$

4.2.1 The Centered Difference Scheme

The first-order derivative centered-difference scheme is a finite-difference method for calculating the effect of fluxes between cells. These schemes have very little dissipation when compared to the Godunov-type discretization, on the other hand without an added artificial diffusion term, the finite-difference scheme is unstable. The first-order derivative centered-difference scheme has the form

$$\frac{\partial \Phi}{\partial x} = \frac{\Phi_{i+1} - \Phi_{i-1}}{2\Delta x}. \tag{4.14}$$

When the first-order derivative centered-difference is discretized to follow the form of the implicit LHS matrix 4.12 the hyperbolic terms are

$$a_n(A) = \frac{\Theta}{1+\zeta}\Delta t(\frac{A_{n+1} - A_{n-1}}{\Delta x}),$$
$$b_n(A) = \frac{\Theta}{1+\zeta}\Delta t(\frac{A_n}{2\Delta x}),$$
$$c_n(A) = \frac{\Theta}{1+\zeta}\Delta t(-\frac{A_n}{2\Delta x}).$$

The artificial dissipation is added as a source term on the RHS and is modelled using a fourth-order term,

$$\Delta x^4 \frac{\partial^4}{\partial x^4} U = U_{i+2} - 4U_{i+1} + 6U_i - 4U_{i-1} + U_{i-2}.$$

4.2.2 The HLLE Scheme

The HLLE scheme is a Godunov-type finite-volume scheme [37] in which inter-cellular fluxes are computed through the approximate solution of a Riemann problem. The linearized Riemann solver HLLE [28, 38, 39] is used to compute the flux on each cell interface, then the change in conserved variables is due to the flux entering from the left minus the flux exiting from the right.

$$\frac{\partial \Phi}{\partial x} = \frac{1}{\Delta x}\left(f_{n+\frac{1}{2}} - f_{n-\frac{1}{2}}\right) \tag{4.15}$$

$$f_{n+\frac{1}{2}} = \begin{cases} F_{n+1}, & \text{if } \lambda_{n+1} < 0 \\ F_n, & \text{if } \lambda_n > 0 \\ \frac{\lambda_{n+1}F_n\lambda_n F_{n+1}}{\lambda_n - \lambda_{n+1}} + \frac{\lambda_{n+1}\lambda_n}{\lambda_{n+1}-\lambda_n}(U_{n+1} - U_n), & \text{otherwise} \end{cases} \tag{4.16}$$

$$f_{n-\frac{1}{2}} = \begin{cases} F_n, & \text{if } \lambda_n < 0 \\ F_{n-1}, & \text{if } \lambda_{n-1} > 0 \\ \frac{\lambda_n F_{n-1}\lambda_{n-1}F_n}{\lambda_{n-1} - \lambda_n} + \frac{\lambda_n\lambda_{n-1}}{\lambda_n-\lambda_{n-1}}(U_n - U_{n-1}), & \text{otherwise} \end{cases} \tag{4.17}$$

$$\lambda_{n+\frac{1}{2}} = \max\left(U_{n+\frac{1}{2}} + \sqrt{\gamma\frac{p_{n+\frac{1}{2}}}{\rho_{n+\frac{1}{2}}}}, \tilde{U} + \sqrt{\gamma\frac{\tilde{p}}{\tilde{\rho}}}\right) \tag{4.18}$$

$$\lambda_{n-\frac{1}{2}} = \max\left(U_{n-\frac{1}{2}} - \sqrt{\gamma\frac{p_{n-\frac{1}{2}}}{\rho_{n-\frac{1}{2}}}}, \tilde{U} - \sqrt{\gamma\frac{\tilde{p}}{\tilde{\rho}}}\right) \tag{4.19}$$

Here a overtilde $\tilde{\varphi}$ indicates the variable evaluated at the Roe-averaged state $\tilde{\varphi}_n = \frac{\sqrt{\rho_{n-\frac{1}{2}}}\varphi_{n-\frac{1}{2}} + \sqrt{\rho_{n+\frac{1}{2}}}\varphi_{n+\frac{1}{2}}}{\sqrt{\rho_{n-\frac{1}{2}}} + \sqrt{\rho_{n+\frac{1}{2}}}}$ with the exception density itself to be $\tilde{\rho} = \sqrt{\rho_{n+\frac{1}{2}}\rho_{n-\frac{1}{2}}}$. One can also notice, since this solver will only be solving subsonic flows, the first two cases in Equation 4.16 and 4.17 are never encountered. Reforming this into the template laid out in this section leads to,

$$a_n(A) = \frac{\Theta}{1+\zeta}\Delta t\frac{1}{\Delta x}\left(\frac{\lambda_{n-1}}{\lambda_n - \lambda_{n-1}}A_n - \frac{\lambda_n\lambda_{n-1}}{\lambda_n - \lambda_{n-1}}I + \frac{\lambda_{n+1}}{\lambda_{n+1} - \lambda_n}A_n - \frac{\lambda_{n+1}\lambda_n}{\lambda_{n+1} - \lambda_n}I\right)$$

$$b_n(A) = \frac{\Theta}{1+\zeta}\Delta t\frac{1}{\Delta x}\left(\frac{\lambda_n}{\lambda_{n+1} - \lambda_n}A_{n+1} - \frac{\lambda_{n+1}\lambda_n}{\lambda_{n+1} - \lambda_n}I\right)$$

$$c_n(A) = \frac{\Theta}{1+\zeta}\Delta t\left(\frac{\lambda_n}{\lambda_n - \lambda_{n-1}}A_{n-1} - \frac{\lambda_n\lambda_{n-1}}{\lambda_n - \lambda_{n-1}}I\right)$$

To attempt achieving second-order accuracy without paying for pentadiagonal matrix inverse, the Van Albada flux limiter [41] is only implemented on the RHS of the equations.

4.2.3 Numerical Configuration

As the estimation to the solution of an implicit method converges, the magnitude of the stable time-step increases. Initial condition that are as close to the solution should be set to accelerate convergence of the one-dimensional solutions. To do this, the solution of the method detailed in Section 4.1 is used as initial condition, since the solution at higher flame Mach numbers is not fully defined by the above method, the same shooting method for non-reactive set of equation is done using the burned state as initial conditions and matched at some point in the burned region. This gives a good approximation as well as setting a minimum of non-realistic discontinuities for the initial conditions.

The stable time-step for an implicit method is unknown. The convergence of the solution can be accelerated by taking time-steps as close as possible to the stable time-step. In the in-house solver a maximum time-step is given by the user. This timestep is used until the solution becomes nonphysical or a certain amount of time in the simulation has passed. If the solution proves to be unstable, then the time-step is reduced and the solution is reset to the previous stable solution.

The Dirichlet boundary conditions are used at both ends equal to the jump conditions given by the Rankine-Hugoniot jump conditions. When the free stream boundary conditions were imposed, the solution showed stability issues when the Arrhenius pre-exponential factor was far from the solution. A domain width of ± 500 is used to solve the one-dimensional flame profiles.

4.2.4 Determination of the Pre-exponential Factor

A given flame velocity can only be simulated if the correct value of the pre-exponential factor is used. Until this value is found accurately, the solution of the flame that is found is a flame profile not propagating at the wanted speed. For example, increasing the value of this parameter increases the velocity of the flame profile. The goal is to find the value at which the flame does not move in the domain since the frame of reference of the flame was chosen. A simple check at some distance before the

diffusion zone is significant is done to verify the velocity at that location. If the velocity is below one, then the Arrhenius pre-exponential factor is increased while if this value is above one the Arrhenius pre-exponential factor is reduced. A bisection method is used for the convergence of the Arrhenius pre-exponential factor.

4.3 Results

In Figure 4.2(a) and 4.2(b), a comparison of the results of Case 1 for re-dimentionalized pressure $\hat{p} = \frac{p}{\gamma M_1^2}$ and temperature $\hat{T} = \frac{T}{\gamma M_1^2(Q+1)}$ is shown. The quasi-isobaric and CJ deflagration flame profile are similar, but there are two significant differences. The first is the pressure drop after the reaction zone in the CJ deflagration is more than half of the unburned pressure while in the quasi-isobaric case the drop in pressure is less than one percent. The second is that the increase in temperature is more significant in the quasi-isobaric profile due to the lack of pressure drop. Both problem 1 and

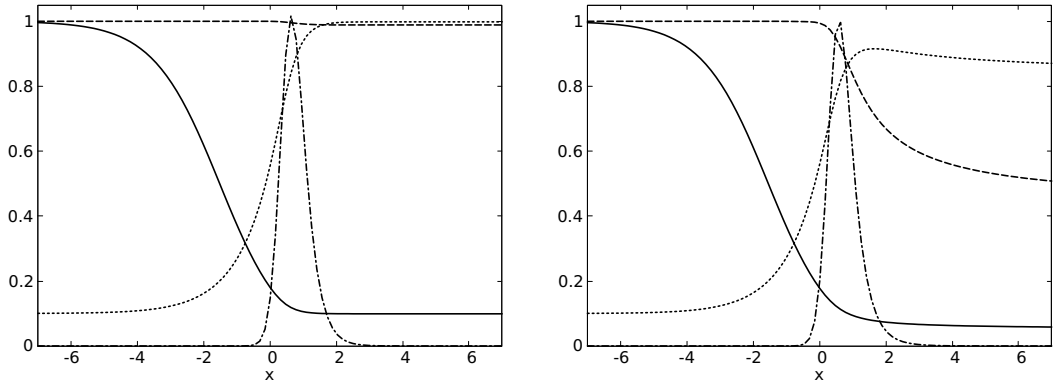

(A) Quasi-Isobaric deflagration (B) CJ deflagration

FIGURE 4.2. Flame structure: Density (——), Pressure (- - - -), Temperature (·····), Reaction Zone (–·–·).

3 have been found using a resolution of 64 cells/δ, while problem 2 and 4 are computed on a coarser mesh with 16 cells/δ. Initially the goal was to compute all cases with a resolution of 64 cells per unit length. Unfortunately, solving the flame profiles of problem 2 and 4 at such high resolutions was not possible due to the decrease in the size of the reaction region, as seen on Figure 4.3, and the increase in the magnitude of the Λ made it extremally difficult to get one-dimensional solutions. Iterating

for the correct Λ became unfeasible. The pre-exponential factors of all 4 problems

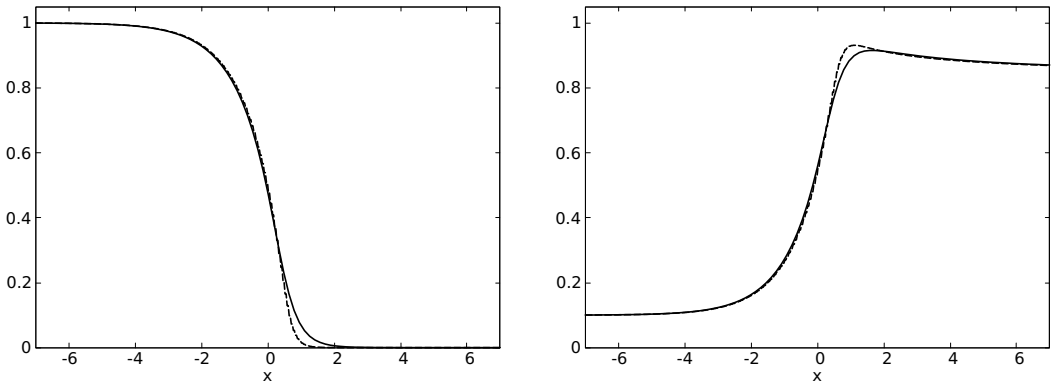

(A) Progress variables profiles (B) Temperature profile

FIGURE 4.3. CJ flame structure: Problem 3 (——), Problem 4 (- - - -).

are compared in Figure 4.4, as expected these values increase with increasing Mach number.

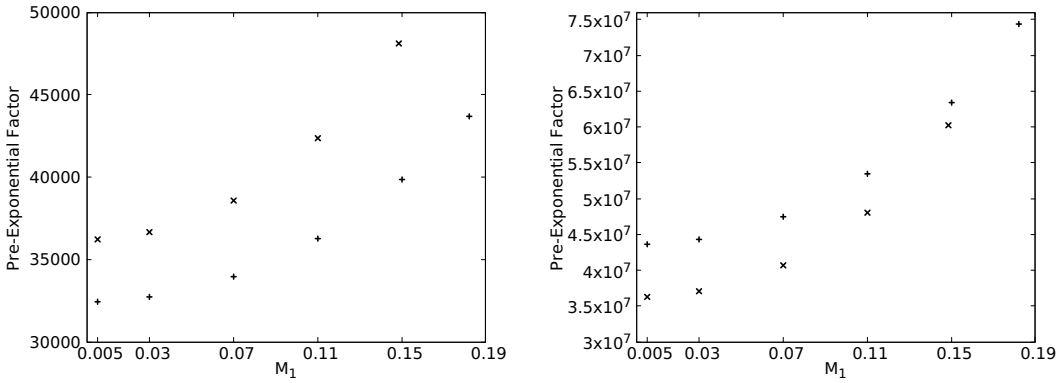

(A) Problem 1 (+) & Problem 3 (∗) (B) Problem 2 (+) & Problem 4 (∗)

FIGURE 4.4. Pre-exponential values.

4.4 Verification of Accuracy

The order of accuracy of the solver was confirmed to be second-order using the methods of manufactured solutions. The necessary resolution for an accurate solution to the iteration of the pre-exponential values is also demonstrated.

4.4.1 Manufactured Solutions

The method of manufactured solution is a numerical technique to verify the order of convergence of a numerical solver. Due to the sparsity of analytical solution of the compressible Navier-Stokes equations, a solution to the equation is enforced as function of x. Then a source term is derived from this enforced solution equal to the residual of the Navier-Stokes equations with the enforced solution. This source changes the PDE, such that the chosen functions are the exact solution. The spatial accuracy of the numerical implementation can be verified. In this work, the solution enforced for the manufactured solution is chosen to be $\rho(x) = \frac{-9}{20}\tanh[4x-10] + \frac{55}{100}$, $u = -\rho$, $e = 2\tanh[4x-10] + 70000$ and $Y = -\frac{1}{2}\tanh[x-2] + \frac{1}{2}$. The derivatives of this enforced solution can now be found and fitted into the governing equation of the solver. When this is done for Equation 3.11 - 3.14, a source term of

$$S(x) = S_n \begin{bmatrix} 0 \\ 0 \\ Q \\ -1 \end{bmatrix},$$

where,

$$S_n = \frac{1}{40} e^{\frac{8E_a(11+9\cdot\tanh[10-4x])}{(\gamma-1)(-11198669+\cdot\tanh[10-4x](-769+81\cdot\tanh[10-4x]))}} \Lambda(11+9\cdot\tanh[10-4x](1+\tanh[2-x]))$$

is required to force consistency between the PDE and imposed solution. Figure 4.5 shows the logarithm of the L2 norm compared with the logarithm of number of cells, the in-house implicit solver converges with second-order accuracy in space.

4.4.2 Convergence Study of the Arrhenius Pre-Exponential Factor

Iteration for the value of the Arrhenius pre-exponential factor is a significant goal of finding the one-dimensional solution, finding a discretization where this value is approximately converged is required. Figure 4.6 demonstrates the Arrhenius pre-exponential factor of the solutions of different cell density for both the HLLE scheme and centered-difference scheme for the in-house implicit solver. Convergence of both solutions to a similar pre-exponential factor as cell density increased is expected. The

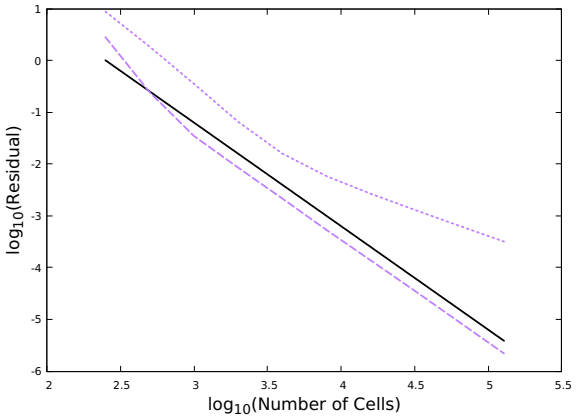

FIGURE 4.5. Spatial convergence plot of manufactured solution: Second-Order Slope (——), Centered-Difference Scheme (- - - -), HLLE Scheme (·····).

convergence of the centered difference scheme converges without oscillatory overshoot of the solution and converges to the final solution at around 64 cells/δ. The HLLE scheme solution oscillates decreasingly to the solution and converges past 128 cells/δ. The centered difference scheme was chosen due to the convergence at a lower resolution, the non-oscillatory behavior of the solution while cell density is increased is also an advantage.

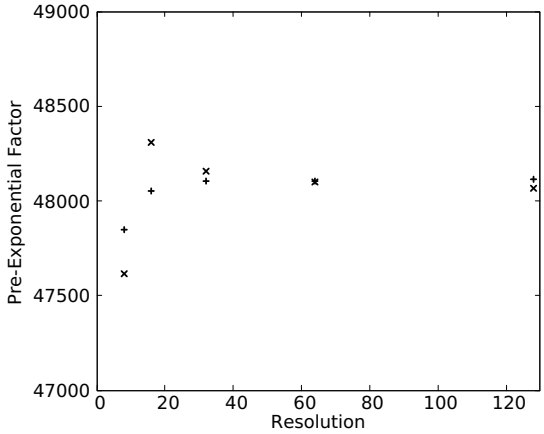

FIGURE 4.6. Space convergence plot of the Arrhenius pre-exponential factor: HLLE (x), Centered-Difference (+).

4.5 Numerical Solution of Isobaric Flames using a Shooting Method

The governing equations from Section 3.1.4 can be reduced to one equation under three simplifications. The first is to neglect the viscosity (τ_{ij}), the second is shown in Liberman *et al.* [9], under some physical assumptions one can consider the thermal conduction and species diffusivity to have similar profile. Finally, to reduce these equations to a one-dimensional spatial problem the steady-state assumption is made. The system of equations is now reduced to

$$\frac{\partial \hat{T}}{\partial x_j} = \frac{\partial^2 \hat{T}}{\partial x_j \partial x_j} + \Lambda(\frac{\hat{T}_2}{\hat{T}} - 1)e^{-\frac{E_a}{\hat{T}}}. \tag{4.20}$$

Then the boundary conditions can be defined as,

$$\begin{aligned} x \to -\infty\,, \qquad & \hat{T} = 1\,, \qquad & \frac{\mathrm{d}\hat{T}}{\mathrm{d}x} = 0\,, \\ x \to \infty\,, \qquad & \hat{T} = 1 + Q\,, \qquad & \frac{\mathrm{d}\hat{T}}{\mathrm{d}x} = 0\,. \end{aligned}$$

The solution to Equation 4.20 can then be solved using a shooting method from the downstream boundary conditions to the upstream boundary conditions. The derivatives can be estimated using a fourth order Runge-Kutta shooting method,

$$\varphi_i^{n+1} = \varphi_i^n + \frac{1}{6}(k_{1i} + 2k_{2i} + 2k_{3i} + k_{4i}),$$

$$k_{1_i} = \Delta x \cdot f_i(x^n, \varphi_j^n),$$
$$k_{2i} = \Delta x \cdot f_i(x^n + \frac{\Delta x}{2}, \varphi_j^n + \frac{k_1}{2}),$$
$$k_{3i} = \Delta x \cdot f_i(x^n + \frac{\Delta x}{2}, \varphi_j^n + \frac{k_{2j}}{2}),$$
$$k_{4i} = \Delta x \cdot f_i(x^n + \Delta x, \varphi_j^n + k_{3j}),$$

where φ_j is a column vector of the primitive variables and the first derivative of $\hat{T}$, $f(x^n, \varphi_j^n)$ are then defined by isolating the derivatives of Equation 4.20, doing so gives us,

$$f(x, \hat{T}, \frac{\partial \hat{T}}{\partial x}) = \begin{bmatrix} \frac{\partial \hat{T}}{\partial x} + \Delta x \frac{\partial^2 T}{\partial x^2} \\ \frac{\partial \hat{T}}{\partial x_j} - \Lambda(\frac{\hat{T}_2}{\hat{T}} - 1)e^{-\frac{E_a}{\hat{T}}} \end{bmatrix}.$$

Once again the value of the Arrhenius pre-exponential factor has to be found through iteration. In this method the solution is solved from the unburned solution to the burned solution. Once the flame profile is solved, if the final temperature is above T_2 then the value of the Arrhenius pre-exponential factor is increased. If the final temperature is below T_2 the value is decreased until the pre-exponential factor is found to the desired accuracy.

4.6 Summary of the One-Dimensional Solutions

In this chapter, an in-depth analysis of two distinct methods to resolve the one-dimensional solution to flames is shown. The shooting method was found to be inadequate to predict the structure of the flames at higher Mach numbers. An implicit solver was necessary to resolve these flame profiles. Not only are the one-dimensional solution tedious and expensive to resolve, the Arrhenius pre-exponential factor has to be found by iteration for the given conditions. In Chapter 6, the one-dimensional solutions that have been found using the implicit solver are used as initial conditions in the two-dimensional cases. Smooth and reliable one-dimensional solution is important to minimize the effect of the initial conditions on the flame profile evolution.

Chapter 5

Isobaric Linear Stability Analysis

As the goal of this thesis is the study of instabilities in flames, information predicting the wavelengths to which the flame is most unstable is useful. This information is used to choose appropriate domain sizes for the multi-dimensional computations. The isobaric linear stability analysis proposed by Liberman *et al.* [9] is chosen, followed by a brief overview of the effects of the extension of this model to the compressible regime by Travnikov *et al.* [13]. Under some approximation shown in Liberman *et al.*, one can consider the thermal conduction and species diffusivity to have similar profiles, the viscosity (τ_{ij}) is also neglected. This relation allows the reduction of one equation in the system posed in Section 3.1.4, where the nondimensional scheme follows Section 3.1.5, the system then appears as

$$\frac{\partial \rho}{\partial t} + \frac{\partial \rho u_j}{\partial x_j} = 0, \tag{5.1}$$

$$\frac{\partial \rho u_i}{\partial t} + \frac{\partial \rho u_i u_j}{\partial x_j} = -\frac{\partial p}{\partial x_i}, \tag{5.2}$$

$$\frac{\partial \rho \hat{T}}{\partial t} + \frac{\partial \rho u_j \hat{T}}{\partial x_j} = \frac{\partial^2 \hat{T}}{\partial x_j \partial x_j} + \rho \Lambda (\hat{T}_2 - \hat{T}) e^{-\frac{E_a}{\hat{T}}}. \tag{5.3}$$

Assuming a quasi-one-dimensional planar flame in a two-dimensional domain, one can predict the growth of small disturbances of a given wavelength by separating perturbations in space with respect to the stable planar flame using the decomposition, $\varphi(t,x,y) = \bar{\varphi}(x) + \tilde{\varphi}(t,x,y)$. Here, $\bar{\varphi}$ is the steady-state planar flame solution, this steady-state solution of the flame is found using the method described in Section 4.5, and $\tilde{\varphi}$ is an imposed two-dimensional disturbance. The dependence of the perturbation on t and y is assumed to behave with the form $\tilde{\varphi}(t,x,y) = \tilde{\varphi}(x) e^{(\sigma t + i\kappa y)}$, where φ represents any primitive variable, $\tilde{\varphi}$ is the amplitude of the perturbation, σ is the nondimensional growth rate ($\sigma = \frac{\bar{\sigma}}{\bar{\delta}}$) and κ is the nondimensional wave number ($\kappa = \frac{\bar{\kappa}}{\bar{\delta}}$) of the perturbation where δ has been defined in Section 3.1.4 as

$\delta = \frac{\bar{k}}{\bar{\rho}_1 \bar{u}_1 \bar{c}_p}$. The primitive variables in equations 5.2 and 5.3 can be replaced using their decomposition stated in this paragraph, the equations then have the form,

$$\frac{\mathrm{d}\tilde{j}}{\mathrm{d}x} = KS\frac{\tilde{T}}{\hat{T}^2} = K\frac{\tilde{v}}{\hat{T}}, \tag{5.4}$$

$$\frac{\mathrm{d}\tilde{v}}{\mathrm{d}x} = -KS\frac{\tilde{v}}{\hat{T}} + K\tilde{p} - 2K\hat{T}\tilde{j} - K\tilde{T}, \tag{5.5}$$

$$\frac{\mathrm{d}\tilde{p}}{\mathrm{d}x} = -KS\tilde{j} - K\tilde{v}, \tag{5.6}$$

$$\frac{\mathrm{d}^2\tilde{T}}{\mathrm{d}x^2} - \frac{\mathrm{d}\tilde{T}}{\mathrm{d}x} - \Lambda\frac{\tilde{T}}{\hat{T}^2}(\hat{T}_2 - \frac{E_a}{\hat{T}}(\hat{T}_2 - \hat{T}))e^{-E_a/\hat{T}} = \tilde{j}\frac{\mathrm{d}\hat{T}}{\mathrm{d}x} + KS\frac{\tilde{T}}{\hat{T}} + K^2\tilde{T}. \tag{5.7}$$

The system of equation has been non-dimensionalized using,

$$K = \bar{\kappa}\delta\,, \quad S = \frac{\bar{\sigma}}{\bar{k}\bar{u}_1}\,, \quad \tilde{T} = \frac{\tilde{T}}{\bar{T}_1}\,, \quad \tilde{v} = i\frac{\tilde{u}_x}{\bar{u}_1}\,, \quad \tilde{j} = \frac{\tilde{\rho}\bar{u} + \bar{\rho}\tilde{u}_x}{\bar{\rho}_1\bar{u}_1}\,, \quad \tilde{p} = \frac{\tilde{P} + \tilde{\rho}\bar{u}_x^2 + 2\bar{\rho}\bar{u}_x\tilde{u}_x}{\bar{\rho}_1\bar{u}_1^2}.$$

Equation 5.4–5.7 describes the evolution of the perturbations of the flame. These equations need information about the flame profile to numerically solve this set of four PDEs. The solution to the background flow is found using the method described by Sharpe [10], this method was described in Section 3.1.5.

The perturbations $\tilde{j}, \tilde{u}, \tilde{v}, \tilde{T}$ must vanish at $x \to \pm\infty$, while numerically the boundary has to be imposed at a finite location. Liberman *et al.* [9] proposed that the inequality $|\frac{d(lnT)}{dx}| << \min(1, K)$ is adequate to predict the location at which the flow is far enough from the flame that the solution can be considered unperturbed. Further investigations have shown that the solution to this method is not very sensitive to distance of boundary conditions as long as they are far enough so the solution of the flame can be assumed to be the burned and unburned state. In the perturbed region, the perturbation is assumed to be the superposition of exponentials of the form $\tilde{\varphi}(x) = \tilde{\varphi}e^{\mu x}$, where the growth rates in the burned region are restricted under the assumption that they must decay ($\mu > 0$) and in the unburned flow the growth rates must increase ($\mu < 0$). A solution of these perturbed can be found by using the burned boundary conditions or the unburned boundary conditions. Notice that the derivative of the perturbed variable have the form $\frac{\partial\tilde{\varphi}}{\partial x} = \mu\tilde{\varphi}$, substituting this

derivative into Equation 5.4 to 5.7, the system of equations simplifies to four linear equations,

$$\mu\tilde{j} = KS\frac{\tilde{T}}{\hat{T}^2} - K\frac{\tilde{v}}{\hat{T}}, \tag{5.8}$$

$$\mu\tilde{v} = -KS\frac{\tilde{v}}{\hat{T}} + K\tilde{p} - 2K\hat{T}\tilde{j} - K\tilde{T}, \tag{5.9}$$

$$\mu\tilde{p} = -KS\tilde{j} - K\tilde{v}, \tag{5.10}$$

$$\mu^2\tilde{T} - \mu\tilde{T} - \Lambda\frac{\tilde{T}}{\hat{T}^2}(\hat{T}_2 - \frac{\epsilon}{\hat{T}}(\hat{T}_2 - \hat{T}))e^{-\epsilon/\hat{T}} = \tilde{j}\frac{\mathrm{d}\hat{T}}{\mathrm{d}x} + KS\frac{\tilde{T}}{\hat{T}} + K^2\tilde{T}. \tag{5.11}$$

The values of the growth rates μ can be found algebraically by solving for the roots of these four equations. Two roots satisfied the conditions in the unburned region and three roots in the burned region, the roots are described in detail in Liberman *et al.*[9]. These roots are significant as they are a solution of the set of PDEs 5.4–5.7 at which the perturbations $\tilde{T}, \tilde{v}, \tilde{u}, \tilde{j}$ grow proportionally to each other in areas where the flow is at the burned or unburned state respectively to the roots locations. While the background flow is in the partially burned region, the growth rate of each perturbation vary from one-another.

The solution to Equation 5.4–5.7 can then be solved using a shooting method from their respective boundary conditions, found earlier by solving for the roots of the linear system of equations, to the maximum reaction region. The derivatives can be estimated using a fourth order Runge-Kutta shooting method,

$$\varphi_i^{n+1} = \varphi_i^n + \frac{1}{6}(k_{1i} + 2k_{2i} + 2k_{3i} + k_{4i}),$$

$$k_{1_i} = \Delta x \cdot f_i(x^n, \varphi_j^n),$$

$$k_{2i} = \Delta x \cdot f_i(x^n + \frac{\Delta x}{2}, \varphi_j^n + \frac{k_1}{2}),$$

$$k_{3i} = \Delta x \cdot f_i(x^n + \frac{\Delta x}{2}, \varphi_j^n + \frac{k_{2_j}}{2}),$$

$$k_{4i} = \Delta x \cdot f_i(x^n + \Delta x, \varphi_j^n + k_{3_j}),$$

where φ_j is an column vector of the primitive perturbed variables and the first derivative of $\tilde{T}$, $f(x^n, \varphi_j^n)$ are defined by isolating the derivative of Equation 5.4–5.7 gives

us,

$$f(x,\tilde{j},\tilde{v},\tilde{p},\tilde{T},\frac{\partial\tilde{T}}{\partial x}) = \begin{bmatrix} KS\frac{\tilde{T}}{\hat{T}^2} - K\frac{\tilde{v}}{\hat{T}} \\ -KS\frac{\tilde{v}}{\hat{T}} + K\tilde{p} - 2K\hat{T}\tilde{j} - K\tilde{T} \\ -KS\tilde{j} - K\tilde{v} \\ \frac{\partial\tilde{T}}{\partial x} + \Delta x\frac{\partial^2\tilde{T}}{\partial x^2} \\ \frac{\tilde{T}}{dx} + \Lambda\frac{\tilde{T}}{\hat{T}^2}(\hat{T}_2 - \frac{E_a}{\hat{T}}(\hat{T}_2 - \hat{T}))e^{-E_a/\hat{T}} + \tilde{j}\frac{d\hat{T}}{dx} + KS\frac{\tilde{T}}{\hat{T}} + K^2\tilde{T} \end{bmatrix}.$$

Once these equations are solved, two complete superimposed solution can be found using the 3 sets of one-dimensional profiles found from the burned boundary conditions and the 2 sets of one dimensional profile found using the unburned boundary condition. The growth rate for a given wave number can be found when the two superimposed solutions can be matched at some location in the flame, the location of maximum reaction is chosen. There are two problems, the initial magnitude of the perturbation at the boundaries for each root is not known, the solution given by the shooting method at that point is just the information on the linear dependence on all perturbed variables. Also, there are three solutions coming from the burned flow to meet two solutions from the unburned flow. Since the magnitude of any perturbed variable is arbitrary, a linear combination does not need to be found, only that there is a possibility of any linear combination of the three solutions from burned side is linearly dependent to the two solution from the unburned side. This can be attained when the determinant of the 5 by 5 matrix composed of all 5 variable that have to be integrated $(\tilde{T},\tilde{v},\tilde{u},\tilde{j},\frac{\partial\tilde{T}}{\partial x})$ is zero since the determinant of a matrix is zero if the vector solutions is linearly dependent.

The solution to all problems of interest are shown in Figure 5.1, this is useful to gauge at which wavelengths the problem of interest are unstable. On the vertical axis is the dimensional growth rate of the quasi-linear problem for a given wavenumber and on the x-axis is the wavenumber. The analysis shows that for a isobaric flame, the stability is not affected by the energy of activation significantly while it is affected by the increase of heat release. It also shows that Problem 3 and 4 are unstable to more wavelengths than Problem 1 and 2. For this reason, when considering the domain width for the two-dimensional simulations, the wavelength of perturbation is chosen to match the average if both most unstable wavelength ($\kappa \approx 0.19$ or $\lambda \approx 33\delta$).

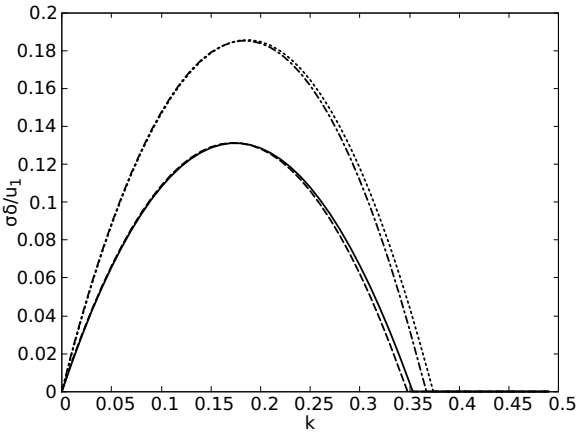

FIGURE 5.1. Isobaric linear stability analysis: Problem 1 (——), Problem 2 (- - - -), Problem 3(·····), Problem 4(–·–·).

Travnikov [13] has extended this model to the compressible regime and has shown that in this regime the growth rate as well as the domain of instability increase with increased compressibility in flames. This means that as Mach number of the flame is increased, it should remain unstable for the given wavelengh. It has also been mentioned that waves tend to propagate at their most unstable mode available, this means that as the flame Mach number is increased, the flame might propagate at a smaller wavelength.

Chapter 6

2D Numerical Scheme and Problem Definition

To simulate and measure the growth rates, two-dimensional simulations have been run. For the 2-D numerical simulation, MG [35], an explicit parallel Godunov-type finite-volume solver written in C++ is used.

6.1 Numerical Software for Two-Dimensional Simulations

MG uses the HLL flux function for the hyperbolic fluxes as well as a second-order finite-difference rule to approximate the second derivatives. This solver utilized cartesian meshes with the ability for adaptive mesh refinement(AMR). The primary refinement criterion MG utilizes is a comparison of solution between mesh levels. The solver compares the solution of a refined mesh to the solution on the above coarsened mesh. If the residual between the meshes level is over a certain criterion, the mesh is refined.

6.2 Initial Conditions

The prescribed initial conditions are a protrusion of the one-dimensional solution across the y-dimension of the domain. In order to excite any instability, an initial perturbation in the x-direction coordinate of the one-dimensional flame profile of the form $A_0 \cos(2\pi y/\lambda)$ where $A_0 = 0.01$ as shown in Figure 6.1.

6.3 Boundary Conditions and Domain Size

The choice of boundary conditions is important for numerical accuracy and to minimize the error they cause in the solution. The numerical boundary has been set as an inflow-outflow problem, the velocity was chosen to have a stationary planar flame in the numerical domain. The isobaric case has been studied extensively by Sharpe

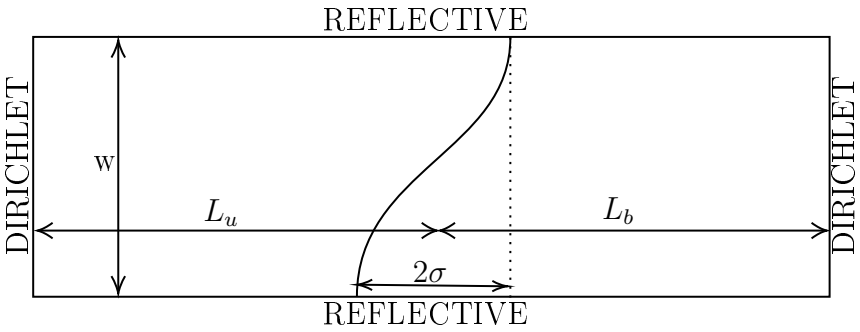

FIGURE 6.1. Initial condition

and Falle [11], the compression waves travel at speeds of approximately $200\frac{\delta}{\tau}$ in the unburned region. The domain length for the boundary condition to be inconsequential would have to be far enough that, during the simulation, the pressure waves do not reach the boundaries, this would be 8000δ in the unburned side, since the simulations in this thesis are ran for 40τ. The burned-side domain would have to be even further away, due to the velocity increase through the flame. Even with AMR, these domains in themselves consume a considerable amount of computation resources. Sharpe and Falle have concluded with simulations that, for isobaric cases, the choice of end boundary conditions does not affect the simulation significantly if a domain of $\pm 2000\delta$ is chosen. A Dirichlet boundary condition is chosen for these boundary conditions and are set to values given by the Rankine-Hugoniot jump conditions. In flames propagating at 10% the velocity of sound, the pressure waves only travel at $10\frac{\delta}{\tau}$. This means only a domain of 400δ is technically necessary for pressure waves not to reach the boundaries in the unburned region and 800δ in the burned region. To verify the effects of the location of the boundary conditions, a set of numerical studies was conducted. Figure 6.2 shows the observed growth rate for Problem 1 at the CJ velocity for domain size of $\pm 500\delta$ compared to the chosen domain of $\pm 2000\delta$. The explanation of how this growth rate of the perturbations is calculated is detailed in Section 7.2. As expected this shows that the solution does not change significantly with the choice of domain size bigger than $\pm 500\delta$. For consistency, all domains have been chosen to span $\pm 2000\delta$.

The choice of boundary conditions bounding the y-direction, or width, of the do-

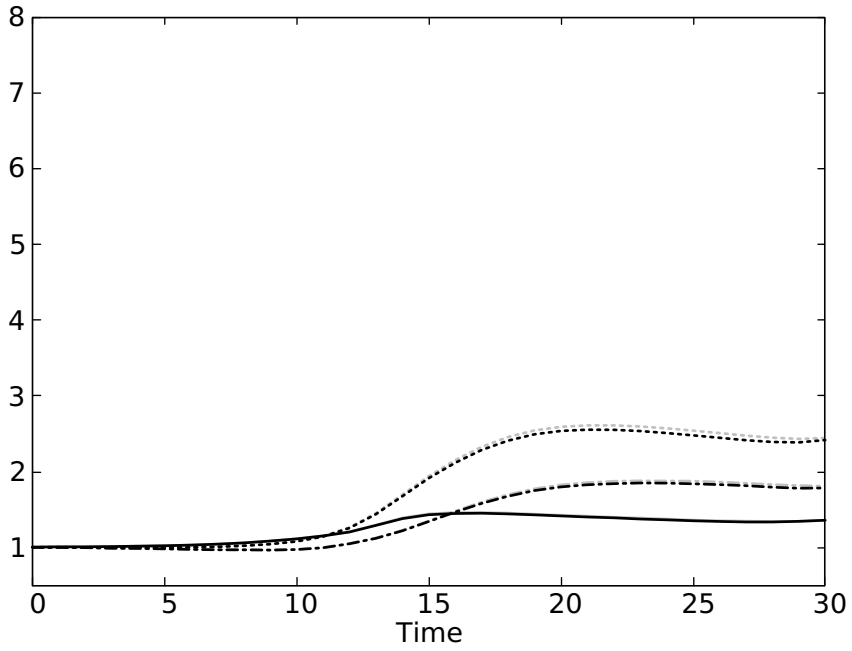

FIGURE 6.2. Growth rate of Problem 1 at the CJ velocity for a domain size of 2000δ in grey and 500δ in black: Flame surface area(——), Flame speed(- - - -), Burning rate(·····).

main are even more complicated, as these flames tend to propagate in cellular-like or cusp-like pattern. Taking into consideration zero gradient, reflective and periodic boundary conditions, their potential effect on the flames is discussed. Now, considering periodic boundary conditions, knowing that flames tend to propagate in cusp-like patterns that repeat in space, using the boundary condition would limit the possible wavelengths in which the cusp-like shapes can evolve to a wavelength that is a multiple of the domain, or $\lambda = w/n$ where n is a natural number. This is due to locking the states on both sides of a boundary to the same value. On the other hand, these boundary conditions would allow for transverse propagation of the cells. However, using reflective boundary conditions unlocks more modes that are half the domain width or $\lambda = w/(2n)$. This allows a domain of half the width to be safely used. There is still the problem that, for a chosen domain width, the propagation of the cellular shape of the flame will change to match the most unstable mode of propagation. Even if a simulation is started with a perturbation of a given wavelength, the evolution of the flame will not explicitly keep that wavelength. The choice of the domain width

is minimized in an attempt to minimize the chance of wavenumber doubling withing the simulations. The most stable case will also be considered, which has been shown by the isobaric linear stability analysis, shown in Chapter 5. The stability analysis has shown that for case 1, the most stable case, the most unstable wavelength to be approximately 33δ or a domain width of 16.5δ. The chosen domain for all simulation is $\pm 2000\delta$ in length and 16.5δ in width using the reflective boundary condition bounding the y-direction and the Dirichlet boundary conditions at both other boundaries conforming to the Rankine-Hugoniot jump conditions.

6.4 Resolution Study

Even with AMR, every time a level of refinement is added, the computational time quadruples due to half of the computational cells being in the most refined state due to the size of the refined region and the maximum time step for the equation is on the order of Δx^2 due to the second derivatives in the Navier-Stokes equations. The final refinement criteria selected give a base cell density of 8 cells/δ with 2 level of refinement for a maximum cell density of 32 cells/δ. This cell density is enforced in the solution field when $Y > 0.001$ or $Y < 0.99$ to ascertain that the reaction zone is fully refined. The solver also uses a multi-level mesh comparison to refine in locations where more cell density is required. The mesh has been visualized for Problem 1 at the CJ velocity at time 0, 10, 20, 30 and 40 respectively in Figure 6.3. These solutions can be compared with Figure 7.1(e) to see the location of the cell refinement in comparison the density profile. The effect of this limited resolution has been studied, Figure 6.4 shows the growth rate predicted with 2 level of refinement as compared with the solution of 3 level of refinement. The resolution study shows that increasing the resolution causes the growth rates to be amplified. Sharpe and Falle [11] also showed a similar effect for isobaric flames, that cells in his most refined solution had a higher peak temperature in the convex section of the flame. This has, as an effect, a higher temperature dissipation and in return a faster growth rate.

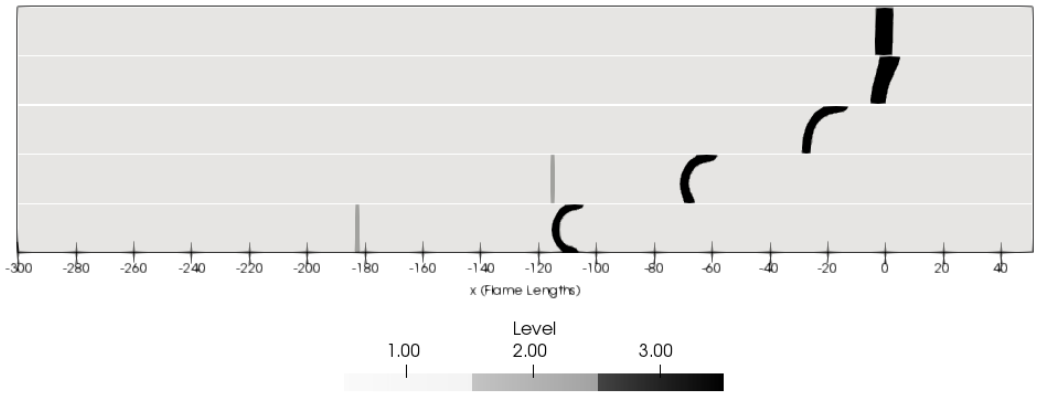

FIGURE 6.3. Level of refinement for Problem 1 at the CJ velocity at time 0, 10, 20, 30 and 40.

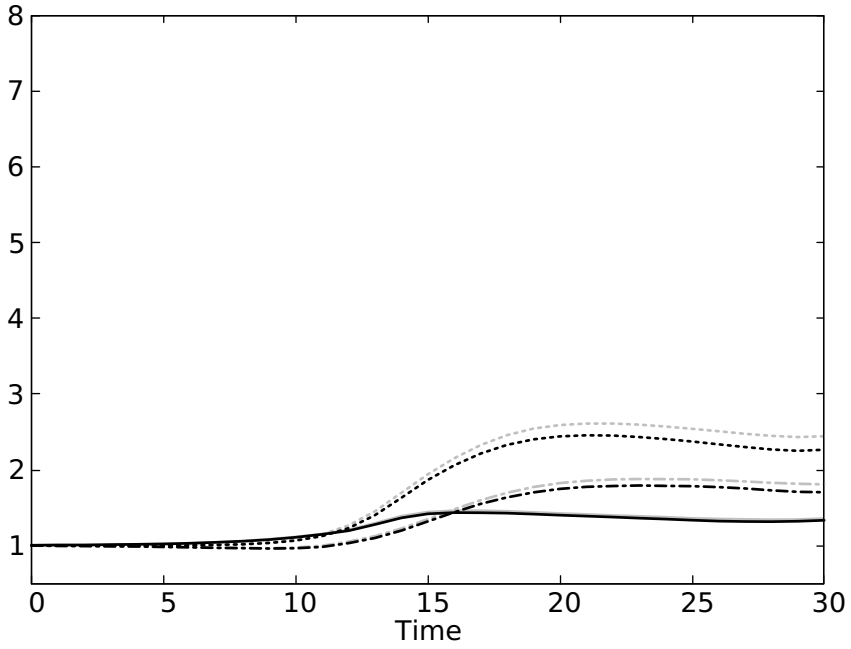

FIGURE 6.4. Growth rate of Problem 1 at the CJ velocity for 32 cells/δ in grey and 16 cells/δ in black: Flame surface area(——), Flame speed(- - - -), Burning rate(·····).

Chapter 7

Analysis of Results

Using the two-dimensional numerical framework described in the previous chapter, numerical solution of the four problems of interest are examined. First, the flame profiles are shown to familiarize the reader to the evolution pattern of a deflagration as modelled in this thesis. It is often shown that, for isobaric flames, the velocity of the flame is proportional to its surface area. This correlation is evaluated in compressible flames and an analysis of the flame velocity in different frames of reference is compared to its surface area. Then an analysis of the growth rate of the flame is done to illustrate the compressible effects and their dependence on the heat release of reaction and energy of activation. Finally, special consideration is given to vorticity. This will be including an analysis of the vorticity equations and each term in the equation.

7.1 Flame Profiles

Figures 7.1–7.4 show the evolution of density of Problem 1–4 at time 0, 10, 20, 30 and 40 except for Problem 2 and 4 at the CJ deflagration velocity, where the plots are at time 0, 1, 2, 3, 4. Some flames did not show any instability within the given simulation time.

The typical evolution of the unstable flames is as follows: the flame is initialized in the quasi-linear state as described in Section 6.2. Then, in time, the flame evolves into a quasi-steady state profile with the initial wavelength. Some flames, however, especially at higher flame velocities or activation energy, evolve to a wavelength that is equal to half of the initial wavelength. Before doing so, these flames seem to be locally stable in time for a short period of time. The CJ case for Problem 2 and 4 quickly transition to detonations. Since the domain is restricting wavelengths other than $w/2n$, and as the flame velocity is increased the most unstable wavelength becomes smaller [13]. The wavenumber doubling for the faster flames is to be expected as it

was shown that the instability of smaller wavelength is increased as the velocity of the flame is increased.

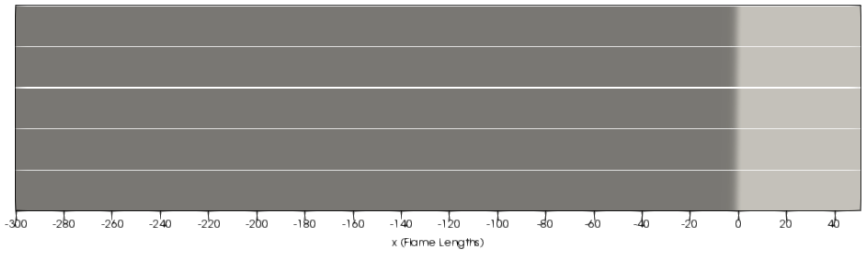

(A) $M_f = 0.03$

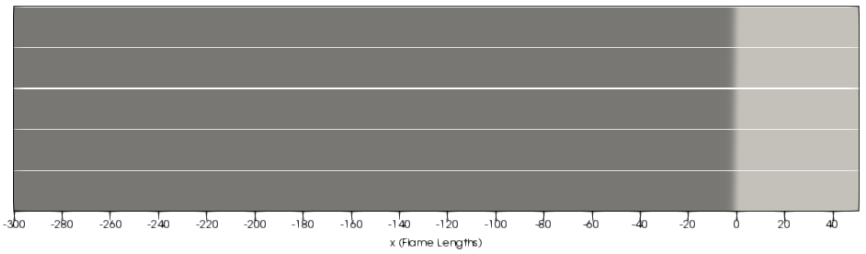

(B) $M_f = 0.07$

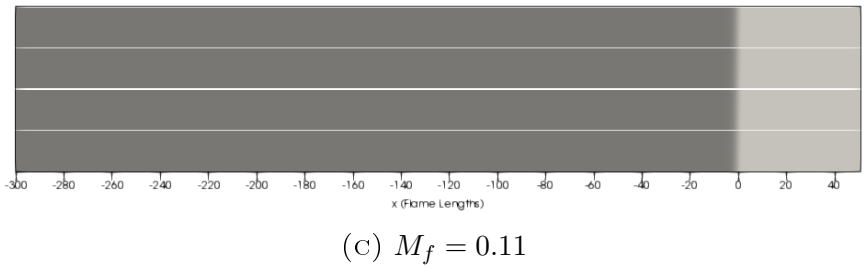

(C) $M_f = 0.11$

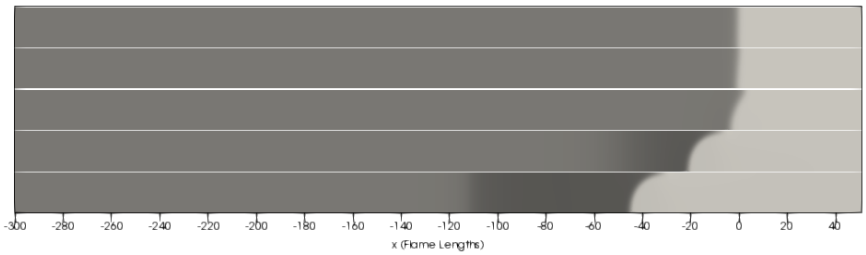

(D) $M_f = 0.15$

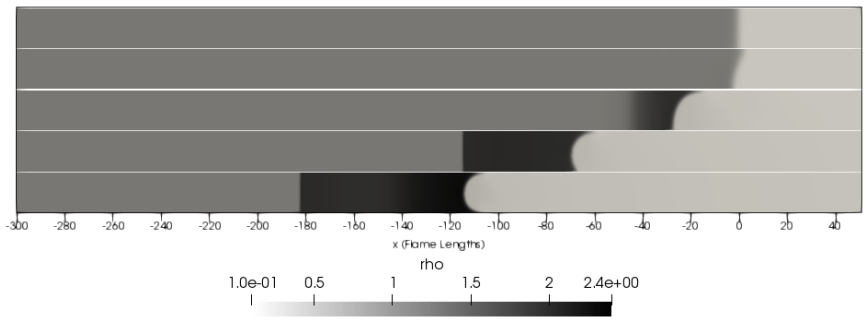

(E) $M_f = 0.18028$

FIGURE 7.1. Problem 1 density evolution

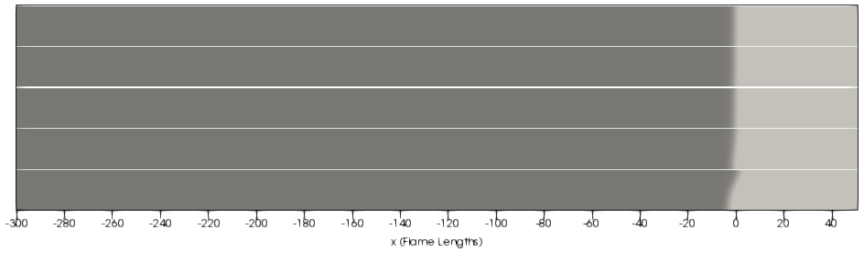

(A) $M_f = 0.03$

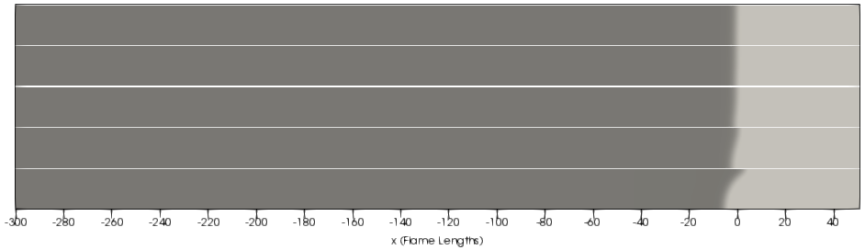

(B) $M_f = 0.07$

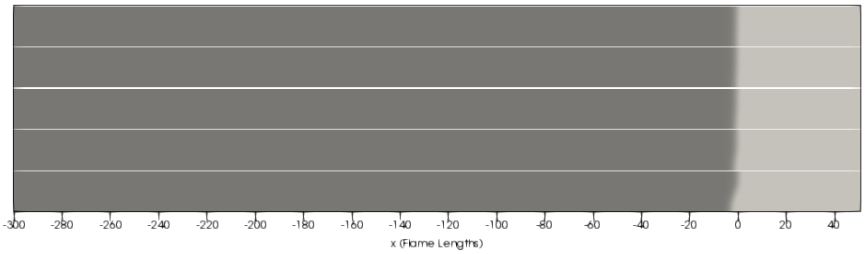

(C) $M_f = 0.11$

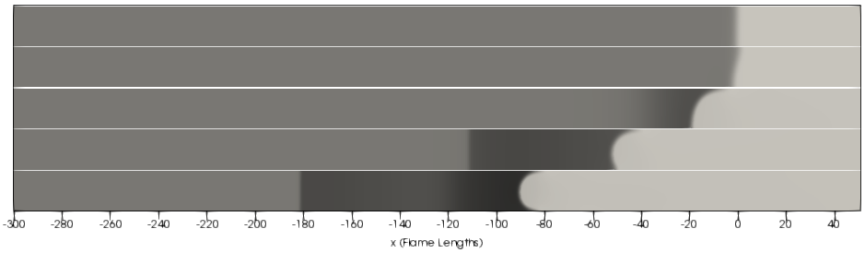

(D) $M_f = 0.15$

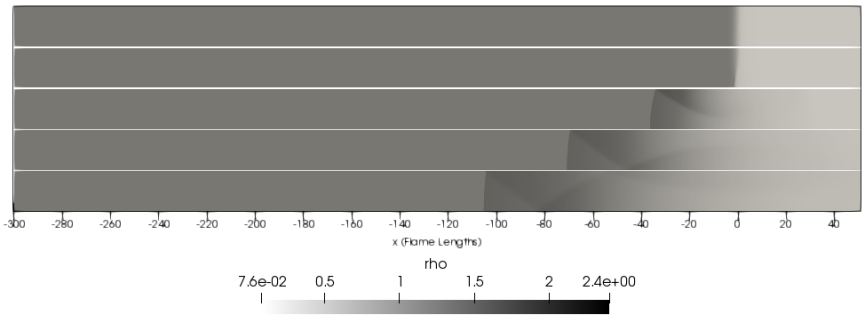

(E) $M_f = 0.18028$

FIGURE 7.2. Problem 2 density evolution

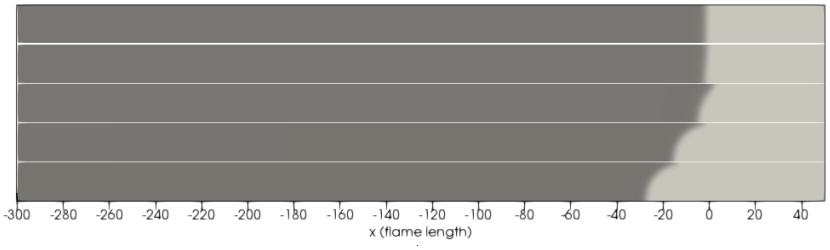

(A) $M_f = 0.03$

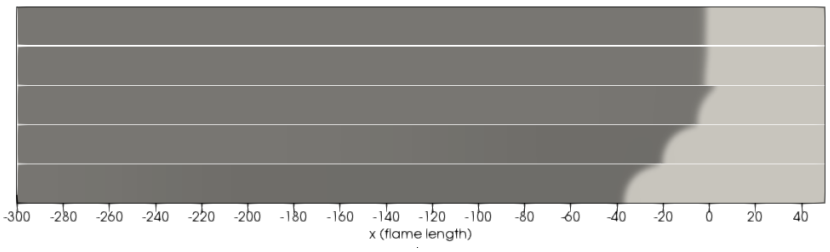

(B) $M_f = 0.07$

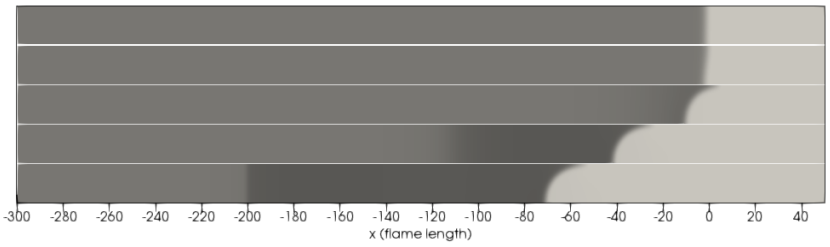

(C) $M_f = 0.11$

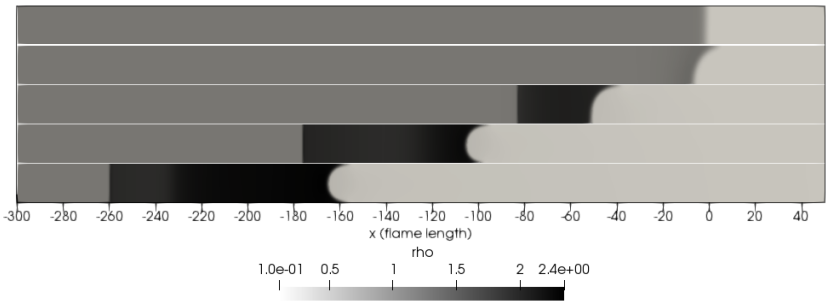

(D) $M_f = 0.148777$

FIGURE 7.3. Problem 3 density evolution

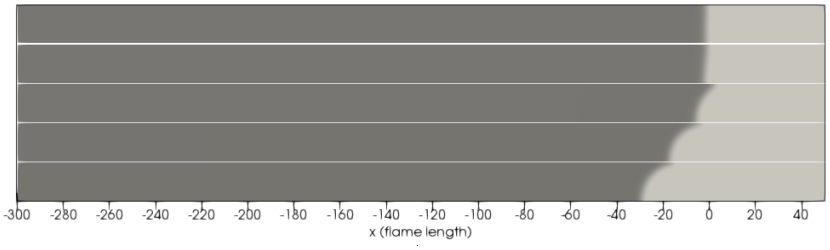

(A) $M_f = 0.03$

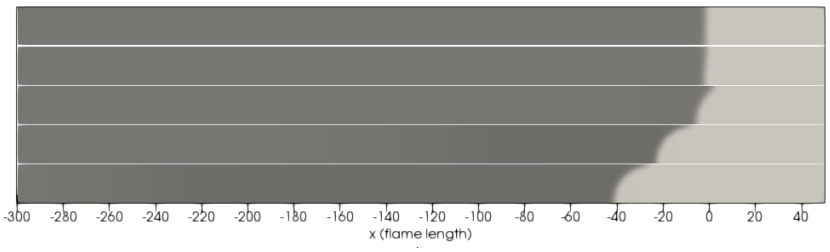

(B) $M_f = 0.07$

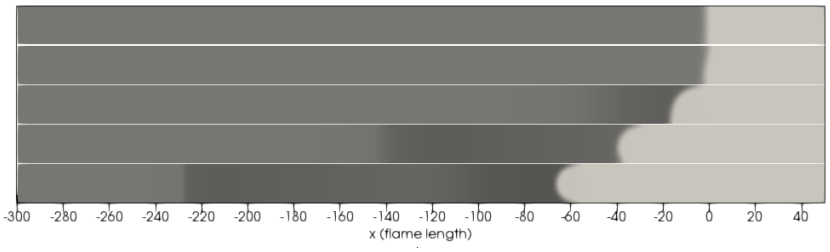

(C) $M_f = 0.11$

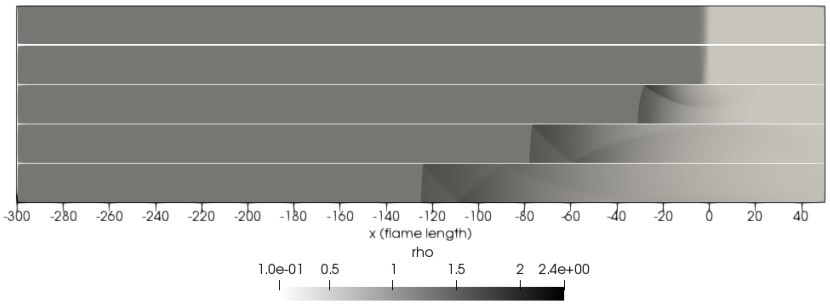

(D) $M_f = 0.148777$

FIGURE 7.4. Problem 4 density evolution

7.2 Propagation of Flames in a Restricted Domain

The previous section demonstrates the evolution of all cases for the 4 problems of interest. The goal now is to investigate and quantify the acceleration of the flame through the domain as the amplitude of cellular flames become important. Figures 7.5–7.8 depict the flame speed at the inlet boundary condition for a flame frame of reference (V_{abs}) for each case. The flame burning rate is calculated from the reaction rate $W_{tot} = \frac{\int\int W dxdy}{w}$, where W is the reaction rate and w is the width of the domain. The plots also contain the flame surface area (A_r) for comparison.

In both the simulation that exhibited DDT, the reaction rate and the propagation speed are the same since all reactants are burned almost instantly at the discontinuity. This discontinuity also travels faster than the speed of sound so the detonation cannot pre-compress upstream gas. Not much interest was paid to these detonations in this thesis as the Arrhenius pre-exponential factor was calculated for deflagration at the CJ velocity encapsulating turbulence on the length scale of the flame length, extrapolation of these assumptions in a flame with a thinner thickness is uncertain.

An important correlation in flames that is often assumed is that the total burning rate is proportional to the surface area of the flame. One can see in Figure 7.5–7.8 that in the quasi-isobaric cases, for the unstable problems (3 and 4), that the reaction rate is indeed proportional to the surface area. While, as compressibility becomes important in flames, the correlation between the flame surface area and the flame reaction rate becomes weaker.

The surface area of the flame diverges from both the flame speed and the reaction rate. Even at the quasi-isobaric flames, a significant accelerating of the gas in front of the flame region is generated convecting the flame forward. This disparity in the correlation between these flame characteristics increases as the compressibility of the flame increases. The reaction rate of the flame, the flame speed and the flame burning velocity with respect to the surface area of all 4 problem at time 40τ is quantified in Table 7.1. The flame burning velocity is defined as $V_{burn} = \frac{\int\int W dxdy}{\rho_2 w}$, where ρ_2 is the width averaged density in front of the reaction region. One can notice that

the divergence of the flame surface area and reaction rate becomes significant in the Problem 3 and 4 around 50 % of the CJ deflagration velocity. When the increase in density of the precompression region is taken in consideration, the burning velocity in respect to the flame surface area can be seen to propagate below the laminar flame velocity. When comparing profiles from Problem 1 and 2 or Problem 3 and 4, the effect of changing the energy of activation in the slow flames is apparent but not as significant as in fast flames.

One can observe from the previous figures that the growth rate of the quasi-isobaric case is much slower than the fast flame. Growth rates for all four problems are shown in Figure 7.9. The plots show the growth rate ($\sigma\delta/u_1$) as defined in the isobaric linear stability analysis, the growth rate of the linear stability analysis is compared in time with the values found in the numerical results. The growth rate was measured using a forward-difference scheme, while the amplitude was measured using the difference between the maximum and minimum location of the reaction. There is a significant increase of growth rate when the flame travels over 50% of its CJ velocity especially once non-linear effects become significant. It is also clear that increasing the energy of activation, when comparing Problem 1 and 2 or Problem 3 and 4, slightly increases the growth rate of the quasi-isobaric flames, but has a more substantial effect on flames in the compressible regime. Increasing the activation energy has shown to accelerate DDT in the simulations. As expected by the linear stability analysis, increasing the heat release of reaction increase the instability of small wavelengths. This is observed when comparing Problem 1 and 2 to Problem 3 and 4, where for low Mach numbers of the problems with the lower heat release of reaction are stable for longer period of time.

7.3 Effect of Compressibility

Compressibility is one of the most significant changes that is apparent in these fast flames, as is seen in Figures 7.1–7.4. The flame curvature quickly propagates pressure waves in front of the flame, in the quasi-isobaric case these pressure wave do not coalesce to the same extent as for the fast flames. This is due to the pressure waves

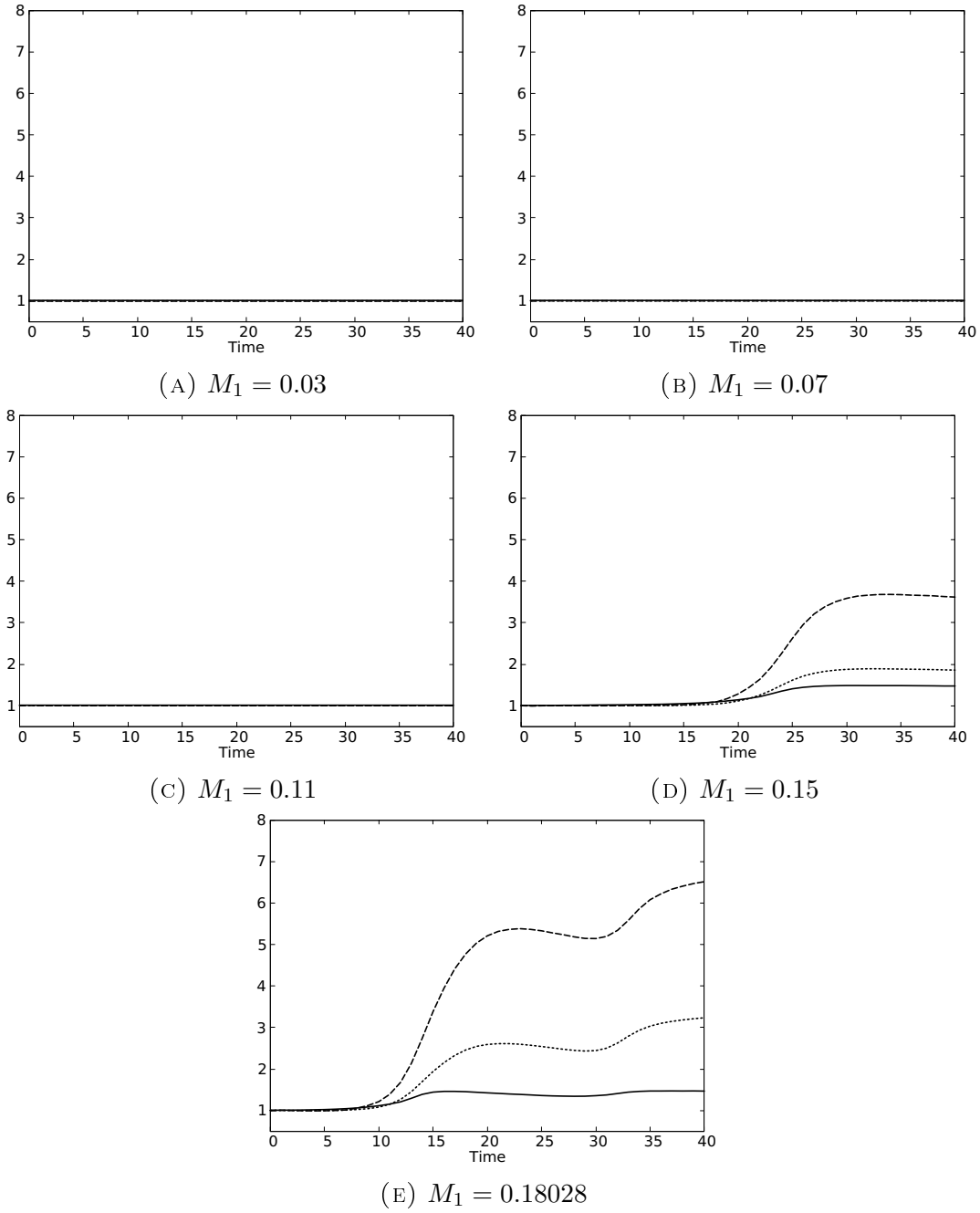

(A) $M_1 = 0.03$ (B) $M_1 = 0.07$

(C) $M_1 = 0.11$ (D) $M_1 = 0.15$

(E) $M_1 = 0.18028$

FIGURE 7.5. Reaction rates of Problem 1: Flame surface area(——), Flame speed(- - - -), Burning rate(·····).

propagating over 5 times faster in front of the flame than for the CJ cases due to the non-dimensional scheme. As flames propagate faster, these precompression regions in front of the flame intensify. These pre-compressed regions then preheat the reactants, accelerate the velocity of the reactants away from the flame and increase the density of

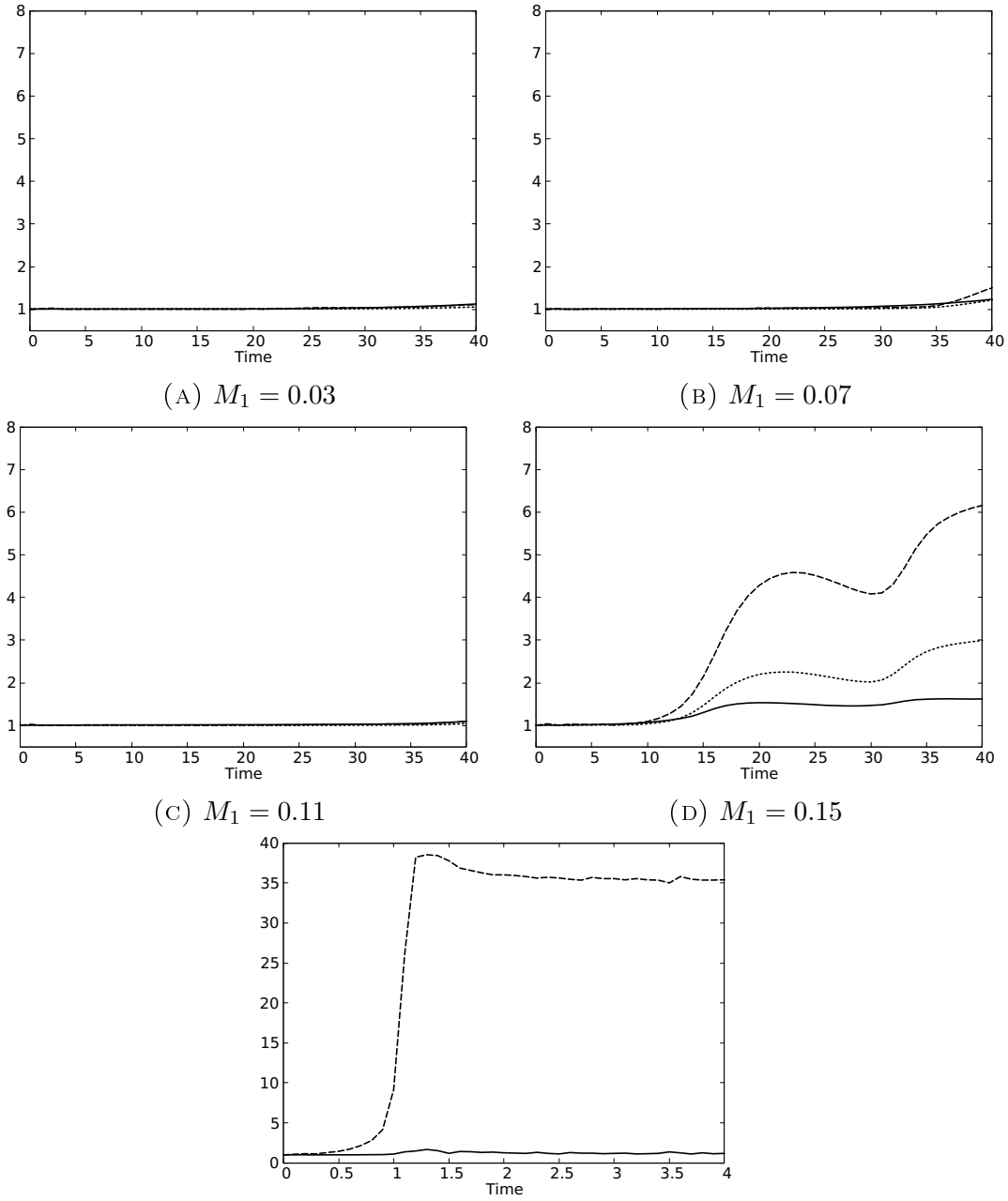

(A) $M_1 = 0.03$

(B) $M_1 = 0.07$

(C) $M_1 = 0.11$

(D) $M_1 = 0.15$

(E) $M_1 = 0.18028$

FIGURE 7.6. Reaction rates of Problem 2: Flame surface area(——), Flame speed(- - - -), burning rate(·····).

the gas. The interaction between these 3 effects and the Darrieus-Landau instability is a very difficult problem to separate since they all affect the growth rate of these cellular profiles simultaneously.

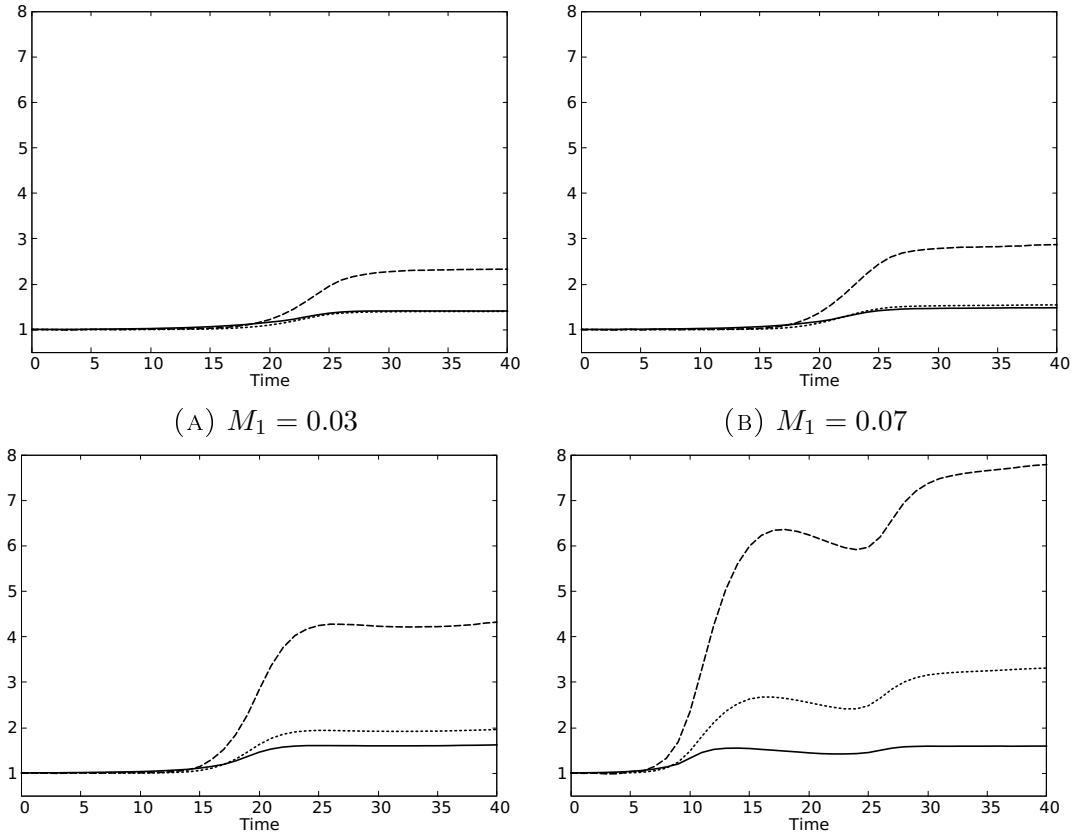

(A) $M_1 = 0.03$ (B) $M_1 = 0.07$

(C) $M_1 = 0.11$ (D) $M_1 = 0.14877$

FIGURE 7.7. Reaction rates of Problem 3: Flame surface area(——), Flame speed(- - - -), Burning rate(·····).

7.3.1 Increase in Temperature

During the initial growth of the cellular structure, the acceleration of the flame creates a precompressed region. This can be observed in Figure 7.10 in the convex section of the flame. In Figure 7.10, the pressure distribution around the reaction region is shown with pressure contour lines overlaid to show the peak of the pressure. The precompression region that is discussed is the darker region following the reaction zone in the convex section of the flame, it is also notable that it has a peak of pressure at that region shown by the pressure contour lines. This is where the cellular growth rate is accelerating as this section of the flame is burning faster than the concave section. This pressure increase in this region is stronger than the one that is to be expected by the DL instability, this is reaffirmed when at later times a discontinuity of pressure

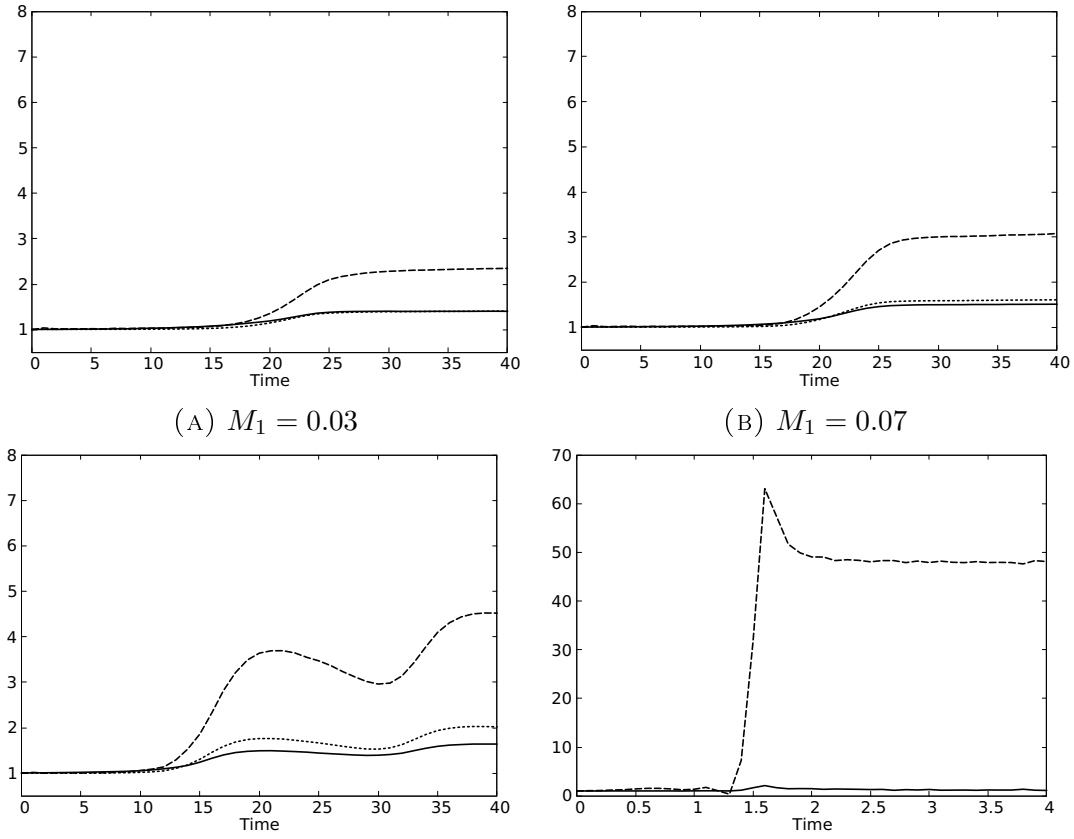

(A) $M_1 = 0.03$ (B) $M_1 = 0.07$

(C) $M_1 = 0.11$ (D) $M_1 = 0.14877$

FIGURE 7.8. Reaction rates of Problem 4: Flame surface area(——), Flame speed(- - - -), Burning rate(·····).

appears in front of the flame created. This is caused by the forward traveling pressure waves. This compression of the unburned reactants on the other hand increases the temperature of the unburned gas allowing for slightly faster combustion, then increasing the growth rate of the cellular flame front. Once the cellular structure developed a stable profile the precompression zone in front of the flame stabilizes but never fully disappears due to the reactant flow profile. One can pose that as the cellular profile accelerates, the flame acts as a piston propagating pressure waves in the reactants, these compression waves increase the temperature in the convex part of the flame. Even if the growth rate increase from this temperature increase is small, the accumulation between a faster growth rate that feeds back into more precompression can eventually increase the reaction rate significantly compared to the quasi-isobaric cases.

TABLE 7.1. Ratio between flame burning rate and flame burning velocity and flame speed over the reaction surface area for the four problems of interest.

7.1(A) Problem 1

M_f	W_{tot}/A_r	V_{burn}/A_r	V_{abs}/A_r
0.03	1.00	1.00	1.00
0.07	1.00	1.00	1.00
0.11	1.00	1.00	1.00
0.15	1.27	0.90	2.46
M_{CJ}	2.26	0.97	4.52

7.1(B) Problem 2

M_f	W_{tot}/A_r	V_{burn}/A_r	V_{abs}/A_r
0.03	0.95	0.96	0.99
0.07	0.97	0.98	1.17
0.11	0.95	0.96	0.99
0.15	1.78	1.02	3.77
M_{CJ}	33.26	33.26	33.26

7.1(C) Problem 3

M_f	W_{tot}/A_r	V_{burn}/A_r	V_{abs}/A_r
0.03	1.00	0.97	1.65
0.07	1.04	0.95	1.93
0.11	1.20	0.90	2.66
M_{CJ}	2.06	0.90	4.86

7.1(D) Problem 4

M_f	W_{tot}/A_r	V_{burn}/A_r	V_{abs}/A_r
0.03	0.95	1.00	1.67
0.07	1.07	0.97	2.04
0.11	1.23	0.91	2.78
M_{CJ}	46.22	46.22	46.22

7.3.2 Convection of the Flame

The previous section demonstrates that there is a precompression region formed in front of the reaction zone. It was also stipulated that these compression waves act like a porous piston and push the reactants in the same direction of the flame. Then, when the flame burns these reactants, the reaction zone also is convected forward by the initial velocity of the flame. This can also be visualized in Figures 7.5–7.8, where the velocity of the flame speed propagates much more quickly than the reaction rate of the flame. The growth rate can also be strengthened by the initial pressure waves from the evolution of the flame profile. As the pressure waves compress the flow in the convex section of the flame, this section of the flames is propagated forward with the unburned gas. The convection has a similar effect as increasing the temperature, it increases the growth rate of the cellular shapes of the flame.

7.3.3 Concentration of Reactants

Finally, due to the flow compression, the density of reactants is increased and the flame has to pre-heat more fuel before combustion can occur. One might expect

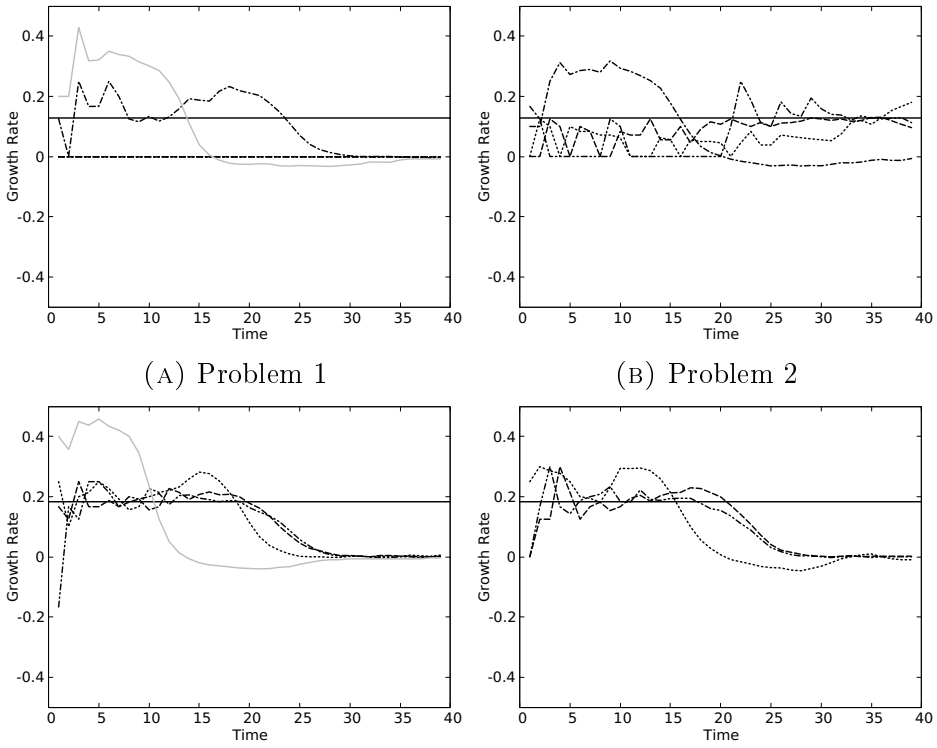

(A) Problem 1 (B) Problem 2

(C) Problem 3 (D) Problem 4

FIGURE 7.9. Growth rate: Linear Stability Analysis (——), $M_1 = 0.03$(– – –), $M_1 = 0.07$(- - - -), $M_1 = 0.11$(·····), $M_1 = 0.15$(– · – ·), $M_1 = CJ$(——).

that the flame would take longer expanding in a denser region, so that the denser pre-compressed area would slow down the growth rate of the cells.

7.4 Vorticity

Due to compressibility and density change, vorticity production is prominent in the flame structure of cellular deflagrations. It is, therefore, expected that vorticity plays a prominent role in flame stability for compressible flames. An analysis of the vorticity as well as the relative magnitude of the terms in the vorticity equation is done for all four problems stated.

Vorticity is an indication of the areas where turbulence is also expected to be prominent [6]. Vorticity defines the local rotation of the fluid compared to the continuum and can be measured using,

$$\omega_i = e_{ijk}\frac{\partial v_k}{\partial x_j}. \tag{7.1}$$

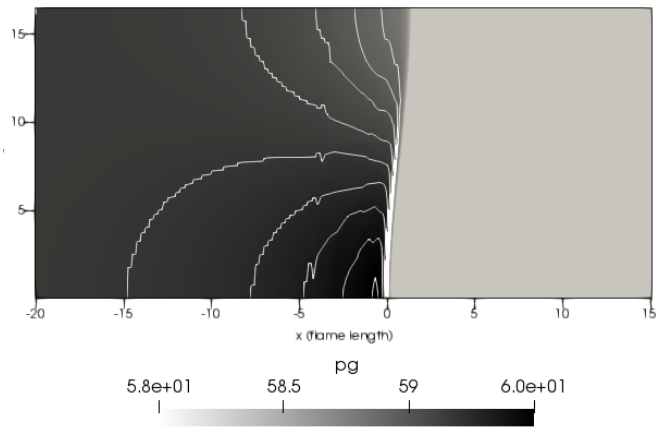

FIGURE 7.10. Pressure profile of CJ deflagration of Problem 3 at 10τ

Since vorticity is a manifestation of angular momentum, one can analyze the evolution for vorticity by taking the curl of the momentum equation, this leads to

$$\frac{\partial \omega_i}{\partial t} = \underbrace{-v_j \frac{\partial \omega_i}{\partial x_j}}_{\text{Convection}} + \underbrace{\omega_j \frac{\partial v_i}{\partial x_j} - \omega_i \frac{\partial v_j}{\partial x_j}}_{\text{Deformation}} + \underbrace{e_{ijk} \frac{1}{\rho^2} \frac{\partial \rho}{\partial x_j} \frac{\partial p}{\partial x_k}}_{\text{Baroclinicity}} + \underbrace{e_{ijk} \frac{\partial}{\partial x_j} (\frac{1}{\rho} \frac{\partial \tau_{km}}{\partial x_m})}_{\text{Viscous}} . \tag{7.2}$$

There are four processes that can lead to a change in the local vorticity. Firstly, the vorticity can be convected by the background flow velocity. Deformation can be important in general, however, in a 2 dimensional flow, the $\omega_j \frac{\partial v_i}{\partial x_j}$ is zero due to vorticity only existing in the z-direction. One can also observe vorticity concentration or dilution due to flow acceleration or deceleration. The baroclinicity is a source of vorticity due to the misalignment of density and pressure gradients. One can imagine that this effect will be more prominent in the compressible regime than the quasi-isobaric regime. One can also have vorticity production due to the viscous stresses, these effects are normally strongest in the boundary layers or shear layers.

Figure 7.11 shows the evolution of the vorticity for Problem 3 at the same times as defined for Figures 7.3. The vorticity in these plots are concentrated on the cusps of the cellular profile, while the convex section of the flame do not have significant vorticity.

Matalon [19] showed that the DL instability also predicts that the vorticity in perturbed flames should have a destabilizing rotation. Figure 7.12 visually depicts this effect, where, on the left the positive rotation of vorticity in this section of the

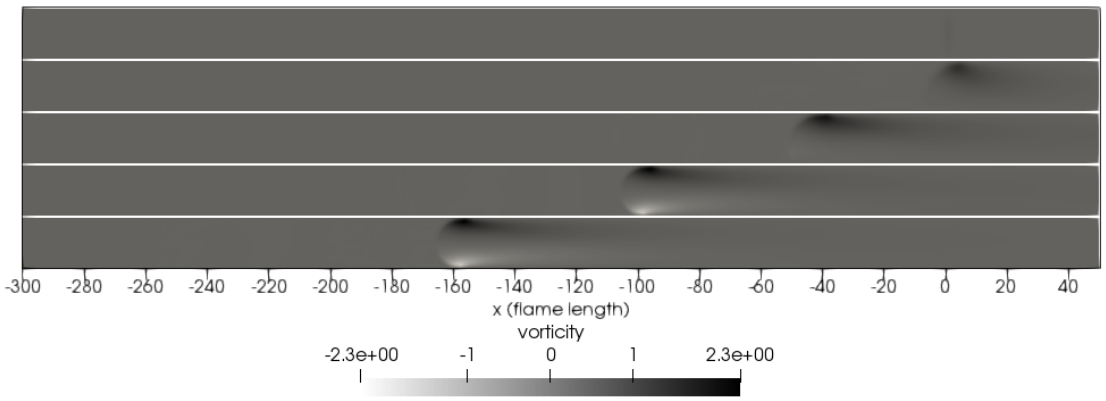

FIGURE 7.11. Vorticity evolution of fast flame for Problem 3

flame would have a stabilizing rotation, while a negative rotation (shown on the right) is expected to have a destabilizing rotation. The solution to the chosen model shows that the vorticity that is predicted, once the flame thickness is taken into consideration, is expected to have a stabilizing rotation.

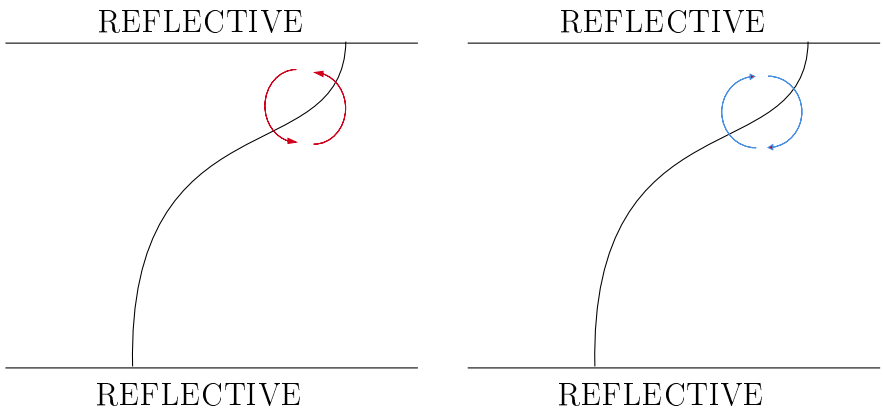

FIGURE 7.12. Vorticity rotation effects on the flame.

It is also interesting to see the effects of each individual term in the evolution equation for the vorticity for the different flame velocities. Figure 7.13–7.16 shows the integral of space

$$\int_{\phi-10}^{\phi+10} \int_{0}^{w} \varphi dy dx \tag{7.3}$$

where φ represents each term in the vorticity equation and ϕ is the location of the flame. This means that the frame of reference is chosen such that the cellular flame is

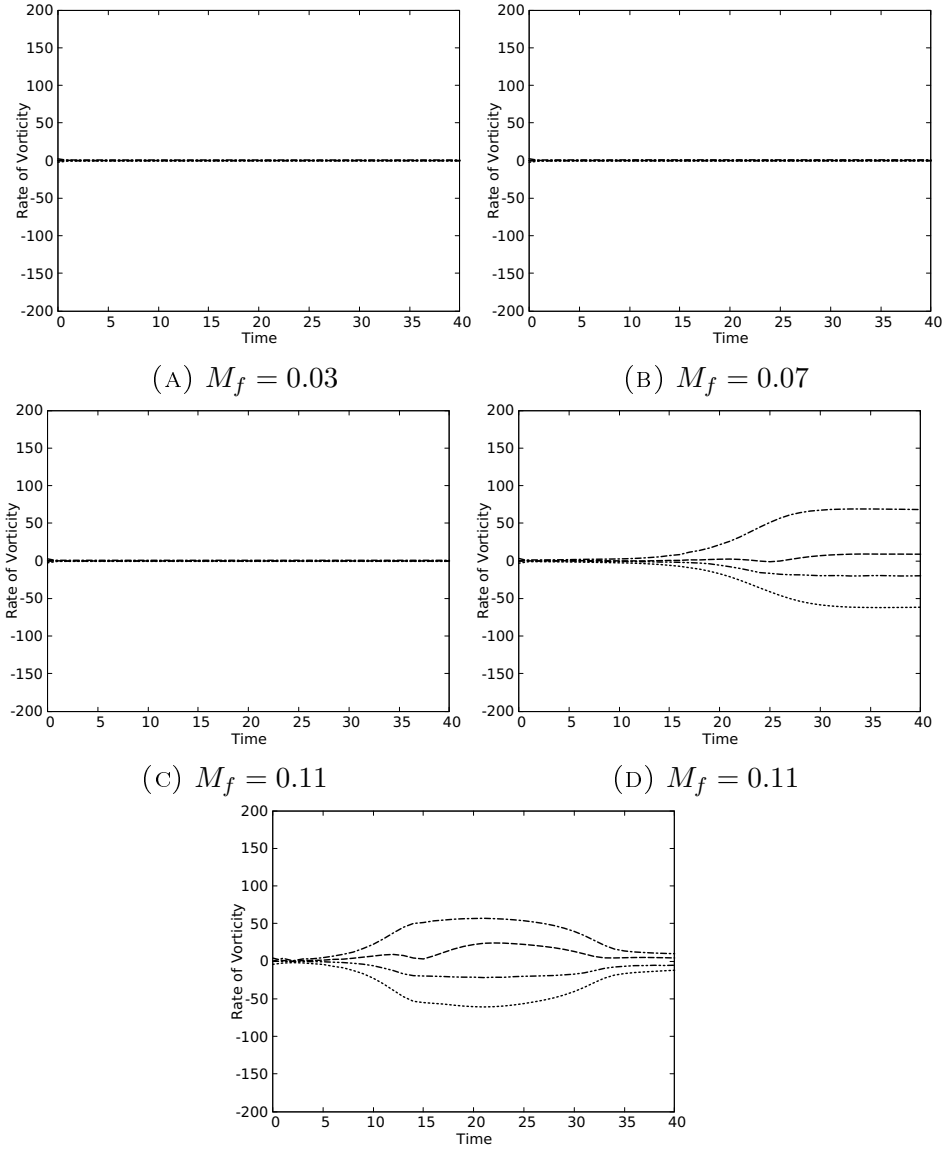

(A) $M_f = 0.03$ (B) $M_f = 0.07$

(C) $M_f = 0.11$ (D) $M_f = 0.11$

(E) $M_f = 0.148777$

FIGURE 7.13. Magnitude of each term in the vorticity equation as a function of time for Problem 1 with flame Mach number 0.03, 0.07, 0.11, 0.15 and M_{CJ}: Convection(- - - -), Baroclinic(– · – ·), Deformation(·····), Viscous(– – – –).

stationary. The flame position is chosen to be the average location on the maximum reaction region in the flame. One can see the general effect of increasing the Mach number of the flame is an increase in vorticity production, one also notice that the convection and the viscous term in the equation are non-zero but have minimal effect on the vorticity when compared to the baroclinic source and the deformation sink.

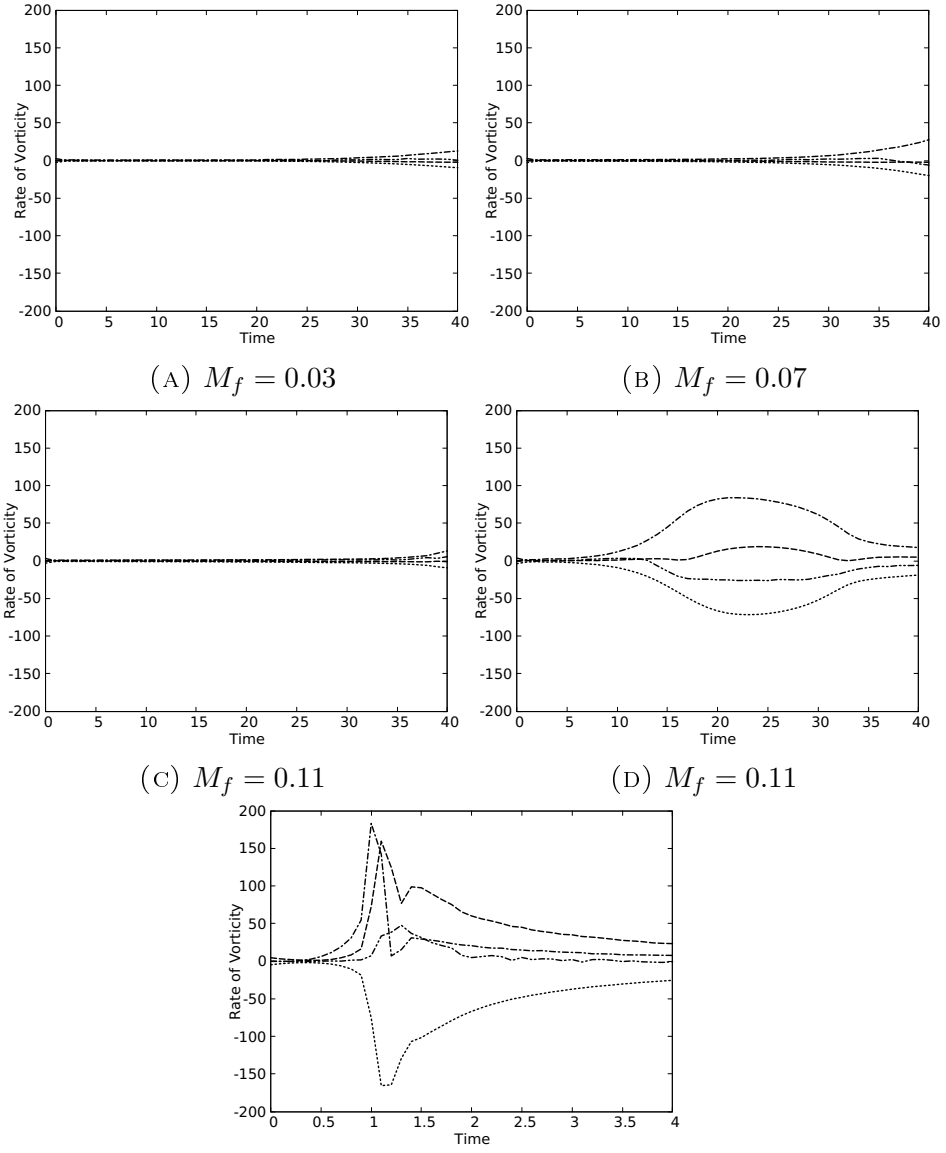

(A) $M_f = 0.03$ (B) $M_f = 0.07$

(C) $M_f = 0.11$ (D) $M_f = 0.11$

(E) $M_f = 0.148777$

FIGURE 7.14. Magnitude of each term in the vorticity equation as a function of time for Problem 2 with flame Mach number 0.03, 0.07, 0.11, 0.15 and M_{CJ}: Convection(- - - -), Baroclinic(– · – ·), Deformation(·····), Viscous(– – – –).

7.4.1 Integral of Vorticity over Flame Amplitude

A strong correlation between the space integral of vorticity and the amplitude of the flame cellular profile has been observed. Figure 7.17 show this for all 4 problems, neglecting any single simulation that became detonations, the total positive vorticity in the domain in the frame of reference following the flame as described in Section

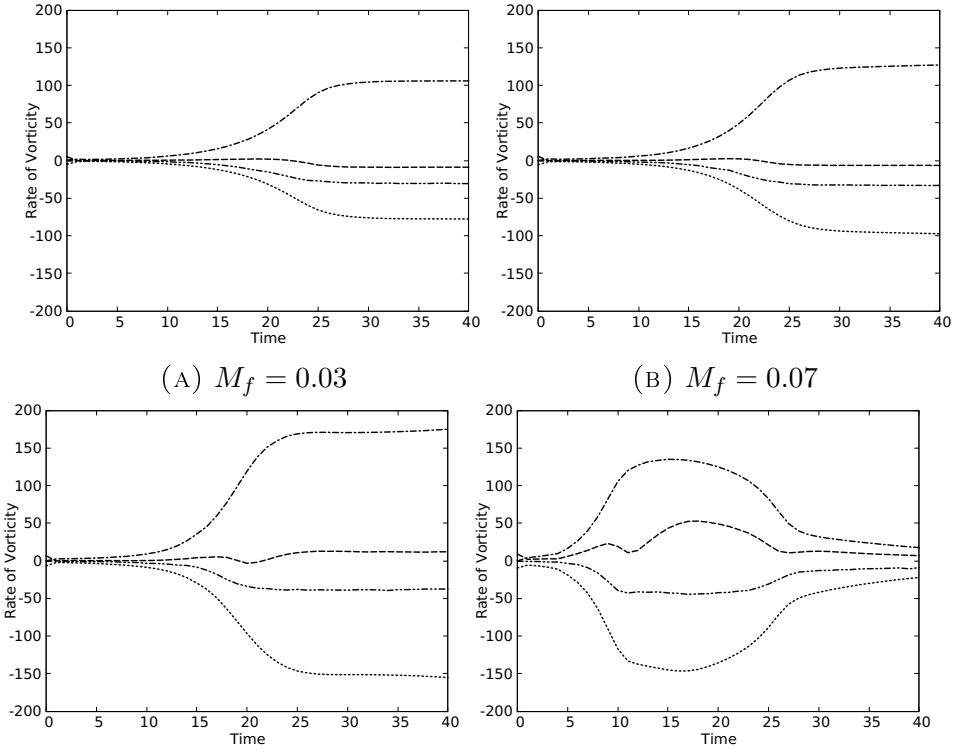

(A) $M_f = 0.03$ (B) $M_f = 0.07$

(C) $M_f = 0.11$ (D) $M_f = 0.148777$

FIGURE 7.15. Magnitude of each term in the vorticity equation as a function of time for Problem 3 with flame Mach number 0.03, 0.07, 0.11 and M_{CJ}: Convection(- - - -), Baroclinic(– · – ·), Deformation(·····), Viscous(– – –).

7.4. Problem 3 is the best example of this phenomena. This is due to the fact that 4 out of 5 flame evolution to a cellular wavelength of half the domain.

The previous section has shown that the vorticity exhibits a stabilizing direction of rotation. While a steady cellular flame is not developed the vorticity is not proportional to the amplitude. One can see in Figure 7.17 that for a given problem and wavelength, the flame can be seen to converge to a ratio between the flame amplitude and the vorticity. This suggests that the vorticity required to stabilize these cellular flames is proportional to the amplitude and constant for a given problem and wavelength. Problem 4 shows a similar evolution of this ratio in the simulations, it also converges to a similar value but slightly higher that Problem 3 where both cases share the same heat release of reaction.

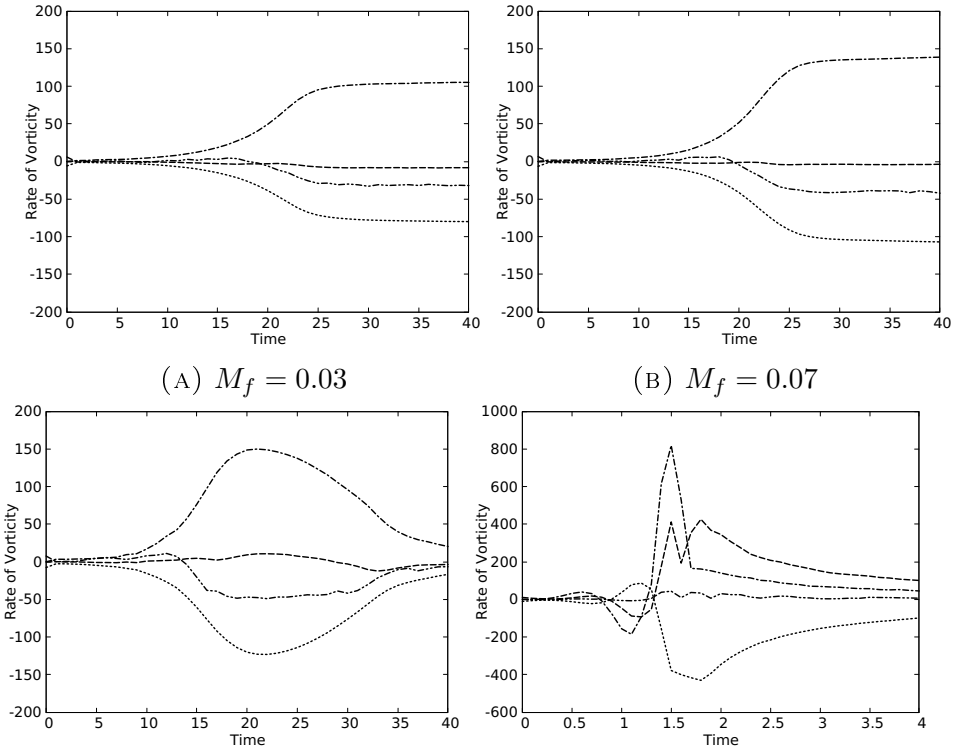

(A) $M_f = 0.03$ (B) $M_f = 0.07$

(C) $M_f = 0.11$ (D) $M_f = 0.148777$

FIGURE 7.16. Magnitude of each term in the vorticity equation as a function of time for Problem 4 with flame Mach number 0.03, 0.07, 0.11 and M_{CJ}: Convection(- - - -), Baroclinic(– · – ·), Deformation(·····), Viscous(– – –).

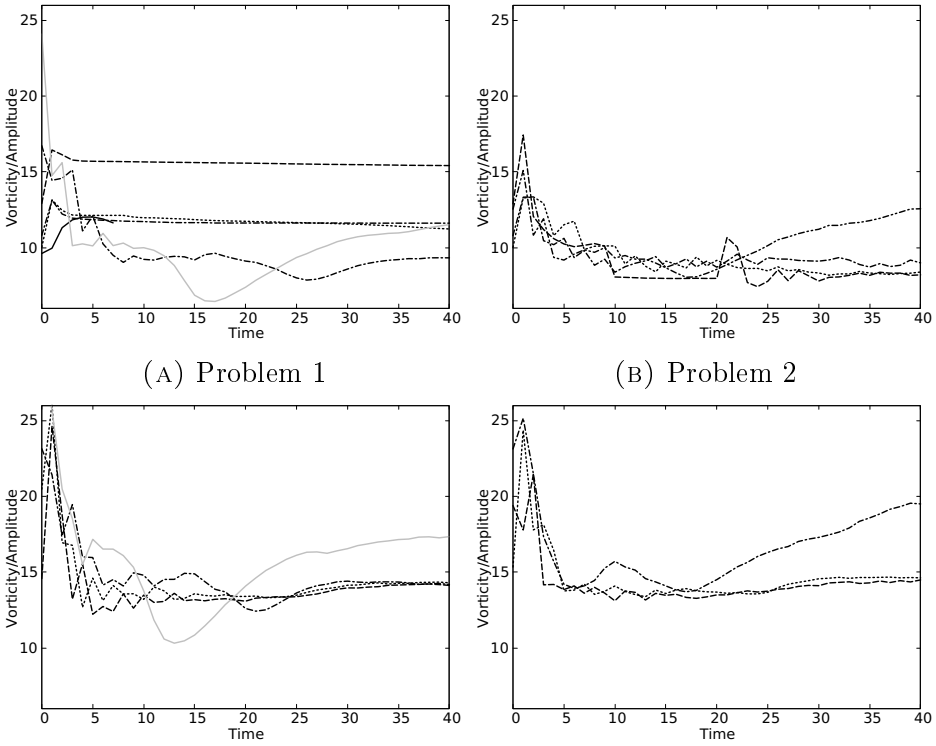

(A) Problem 1 (B) Problem 2

(C) Problem 3 (D) Problem 4

FIGURE 7.17. Ratio between spatial intergral of vorticity and the flame amplitude for all 4 problems: $M_1 = 0.03$(- - - -), $M_1 = 0.07$(– · – ·), $M_1 = 0.11$(·····), $M_1 = 0.15$(– – – –), $M_1 = CJ$(——).

7.5 Summary of the Two-Dimensional Solutions

In this chapter, the simulation results for all 4 problems are shown in the form of density profile. Using these simulations, the correlation of burning flame velocity and flame surface area was shown to be weakened as the compressible effects became significant. The flame was also shown to be convected forward as the burning rate did not match the velocity at which the flame propagated in respect to the unburned gas. It was apparent in the density profiles that compressible flames had faster growth rates that their quasi-isobaric counterpart, these growth rates are quantified in this chapter. This section also discussed the effect that the heat release of reaction and energy of activation has on the flames. As is found in most of the literature on the topic, an increase of heat release of reaction has a significant impact on the stability of the flame while an increase in activation energy has a lesser impact. On the other hand, it was found that the higher activation energy were more susceptible to detonation. The vorticity equation was analyzed and the baroclinic source term was shown to be the dominant source of vorticity in the flames, while the deformation acted as a sink of vorticity, usually on the same magnitude. The sense of rotation in vorticity was opposite as it has been found to have a stabilizing rotation. An analysis of vorticity in respect to the amplitude of the cellular profile then showed that for a given problem and wavelength, this ratio was the same for all flame velocities. This suggests that the vorticity might be a significant stabilizing source in flames. Once the compressibility creates a constant precompression region in front of the flame and the Darrieus-Landau instability is again the primary source of instability, the vorticity in this region only has to negate this effect.

Chapter 8

Conclusion and Future Work

The two-dimensional evolution of fast flames using the Navier-Stokes equations with a one-step chemistry model was investigated. It is found that, compared with the quasi-isobaric flames, fast flames produce a significant precompression region affecting the growth rate of the flames.

The relation between the surface area of the flame and the flame burning rate was accurate for slow flames while it did not hold true in the compressible regime. While the growth rate is always increasing with compressibility, significant change did not occur before the flame were propagating at 50% of the CJ deflagration velocity. The effect of heat release is significant, but similar to the isobaric cases where the growth rate is increased with the increase in heat release. The energy of activation on the other hand seem to have a more significant effect on fast flames. The results also suggest that CJ flames do not stabilize as predicted by Bychkov [17] and He [18]. Three possible cause of the increase of instability due to compressibility are proposed. The first is the increase of reaction rate in the convex section of the flame due to the pre-heating, the second is the convection of the convex section of the flame due to the unburned gas velocity and finally the increase density as a stabilizing effect is proposed.

Further analysis of the vorticity shows that the baroclinic source term is the prominent source of vorticity production in flames and that there is an increase of vorticity as compressibility becomes significant. The vorticity in flames is located at the cusps of the cellular flame profile and it is shown that direction of rotation has a stabilizing rotation. Finally a correlation between the vorticity ratio with the flame amplitude is shown for all four problems, it showed that this ratio at the quasi-steady state of the cellular flames is the same for different flame velocities at some given wavelength, heat release of reaction and energy of activation.

8.1 Future Work

Further analysis could be done for the problems of interest that experienced DDT. Also, the effects of enhancing the realism of the physics could be interesting, including using more detailed chemistry models and turbulence modelling. Three dimensional simulation could also be done, the growth rate in such models would be expected to be higher. Effects of the precompression zone could be quantified in one-dimensional simulation by finding steady-state solution using different inlet boundary conditions. One can pose a one-dimensional solution at which all its properties are self similar to those of the RH Jump conditions while varying the inlet density, velocity and temperature to isolate the effect of such disturbances. A new steady state could be found at a different velocity for this state.

References

[1] B. M. I. I. Board, "Buncefield major incident investigation," *Initial Report to the Health and Safety Commission and the Environment Agency of the investigation into the explosions and fires at the Buncefield oil storage and transfer depot, Hemel Hempstead, on*, vol. 11, 2005.

[2] D. S. Burgess and M. G. Zabetakis, "Detonation of a flammable cloud following a propane pipeline break–the december 9, 1970, explosion in port hudson, mo.," *Bureau of Mines-Report of Investigations*, no. 7752, 1973.

[3] G. Ciccarelli and S. Dorofeev, "Flame acceleration and transition to detonation in ducts," *Progress in Energy and Combustion Science*, vol. 34, no. 4, pp. 499–550, 2008.

[4] E. S. Oran and V. N. Gamezo, "Origins of the deflagration-to-detonation transition in gas-phase combustion," *Combustion and Flame*, vol. 148, no. 1-2, pp. 4–47, 2007.

[5] M. Saif, W. Wang, A. Pekalski, M. Levin, and M. I. Radulescu, "Chapman-Jouguet deflagrations and their transition to detonation," *Proceedings of the Combustion Institute*, vol. 36, no. 2, pp. 2771–2779, 2017.

[6] A. Y. Poludnenko, "Pulsating instability and self-acceleration of fast turbulent flames," *Physics of Fluids*, vol. 27, no. 1, 2015.

[7] A. Eder, F. Pingten, and F. Mayinger, "Propagation of fast deflagrations and marginal detonations in hydrogen–air-additive mixtures," in *Proceedings of 18th international colloquium on the dynamics of explosions and reactive systems, Seattle, Washington*, vol. 181, pp. 29–34, Citeseer, 2001.

[8] W. Rakotoarison, A. Pekalski, and M. I. Radulescu, "Detonation transition criteria from the interaction of supersonic shock flame complexes with different shaped obstacles.," *Journal of Loss Prevention in the Process Industries*, 2019.

[9] Liberman, Bychkov, Golberg, and Book, "Stability of a planar flame front in the slow-combustion regime," *Physical Review. E, Statistical physics, plasmas, fluids, and related interdisciplinary topics*, vol. 49, no. 1, 1994.

[10] G. J. Sharpe, "Linear stability of planar premixed flames: reactive Navier-Stokes equations with finite activation energy and arbitrary Lewis number," *Combustion Theory and Modelling*, vol. 7, pp. 45–65, March 2003.

[11] G. J. Sharpe and S. A. E. G. Falle, "Nonlinear cellular instabilities of planar premixed flames: numerical simulations of the reactive Navier-Stokes equations," *Combustion Theory and Modelling*, vol. 10, pp. 483–514, June 2006.

[12] O. Y. Travnikov, V. V. Bychkov, and M. A. Liberman, "Influence of compressibility on propagation of curved flames," *Physics of Fluids*, vol. 11, no. 9, pp. 2657–2666, 1999.

[13] O. Y. Travnikov, M. A. Liberman, and V. V. Bychkov, "Stability of a planar flame front in a compressible flow," *Physics of Fluids*, vol. 9, no. 12, pp. 3935–3937, 1997.

[14] S. Kadowaki, "Numerical study on lateral movements of cellular flames," *Physical Review E - Statistical Physics, Plasmas, Fluids, and Related Interdisciplinary Topics*, vol. 56, no. 3, pp. 2966–2971, 1997.

[15] S. Kadowaki, "The lateral movement of the three-dimensional cellular flame at low Lewis numbers," *International Journal of Heat and Fluid Flow*, vol. 20, no. 6, pp. 649–656, 1999.

[16] S. Kadowaki, "Numerical study on the formation of cellular premixed flames at high Lewis numbers," *Physics of Fluids*, vol. 12, no. 9, pp. 2352–2359, 2000.

[17] V. Bychkov, M. Modestov, and M. Marklund, "The Darrieus-Landau instability in fast deflagration and laser ablation," *Physics of Plasmas*, vol. 15, no. 3, 2008.

[18] L. He, "Analysis of compressibility effects on Darrieus-Landau instability of deflagration wave," *Europhysics Letters*, vol. 49, no. 5, pp. 576–582, 2000.

[19] M. Matalon, "The Darrieus-Landau instability of premixed flames," *Fluid Dynamics Research*, vol. 50, no. 5, 2018.

[20] J. H. S. Lee, *Detonation Phenomenon*. Cambridge ; New York: Cambridge University Press.

[21] S. Kadowaki, "Numerical study on lateral movements of cellular flames," *Physical Review E*, vol. 56, no. 3, p. 2966, 1997.

[22] R. M. Beam and R. Warming, "An implicit factored scheme for the compressible Navier-Stokes equations.," *AIAA Journal*, vol. 16, no. 4, 1978.

[23] G. Darrieus, "Propagation d'un front de flamme," 1938. La Technique Modèrne (Paris) and in 1945 at Congres de Mécanique Appliquée.

[24] Landau, "The Darrieus-Landau instability in fast deflagration and laser ablation," *Acta Physicochim*, vol. 19, no. 77, 1944.

[25] B. Denet and P. Haldenwang, "Numerical study of thermal-diffusive instability of premixed flames," *Combustion Science and Technology*, vol. 86, no. 1-6, pp. 199–221, 1992.

[26] P. Clavin and F. A. Williams, "Effects of molecular diffusion and of thermal expansion on the structure and dynamics of premixed flames in turbulent flows of large scale and low intensity," *Journal of Fluid Mechanics*, vol. 116, no. -1, pp. 251–282, 1982.

[27] P. Pelce and P. Clavin, "Influence of hydrodynamics and diffusion upon the stability limits of laminar premixed flames," *Journal of Fluid Mechanics*, vol. 124, no. -1, pp. 219–237, 1982.

[28] A. Harten, P. D. Lax, and B. V. Leer, "On upstream differencing and Godunov-type schemes for hyperbolic conservation laws," *SIAM Review*, vol. 25, no. 1, pp. 35–61, 1983.

[29] B. Jarosinski, Jozef; Veyssiere, *Combustion Phenomena: Selected Mechanisms of Flame Formation, Propagation and Extinction*. Boca Raton: CRC Press.

[30] K. Bray and J. Moss, "A unified statistical model of the premixed turbulent flame," *Acta Astronautica*, vol. 4, no. 3, pp. 291–319, 1977.

[31] R. Bilger, S. Pope, K. Bray, and J. Driscoll, "Paradigms in turbulent combustion research," *Proceedings of the Combustion Institute*, vol. 30, no. 1, pp. 21–42, 2005.

[32] J. Buckmaster, *The Mathematics of Combustion*. Society for Industrial and Applied Mathematics, 1985.

[33] N. Peters, *Turbulent Combustion*. Cambridge Monographs on Mechanics, Cambridge University Press, 2000.

[34] S. Yu and S. Navarro-Martinez, "Modelling of deflagration to detonation transition using flame thickening," *Proceedings of the Combustion Institute*, vol. 35, no. 2, pp. 1955–1961, 2015.

[35] S. A. E. G. Falle and J. R. Giddings, "Body capturing using adaptive cartesian grids, in numerical methods for fluid dynamics iv," pp. 337–343, 1993.

[36] H. Pitsch, "Large-eddy simulation of turbulent combustion," *Annual Review of Fluid Mechanics*, vol. 38, no. 1, pp. 453–482, 2006.

[37] S. Godunov, "A difference scheme for numerical computation of discontinuous solution of hyperbolic equation," *Math. Sbornik*, vol. 47, pp. 271–306, 1959.

[38] A. Harten, "High resolution schemes for hyperbolic conservation laws," *Journal of computational physics*, vol. 49, no. 3, pp. 357–393, 1983.

[39] B. Einfeldt, "On Godunov-type methods for gas dynamics," *SIAM Journal on Numerical Analysis*, vol. 25, no. 2, pp. 294–318, 1988.

[40] M. Radulescu, G. Sharpe, J. Lee, C. Kiyanda, A. Higgins, and R. Hanson, "The ignition mechanism in irregular structure gaseous detonations," *Proceedings of the Combustion Institute*, vol. 30, no. 2, pp. 1859–1867, 2005.

[41] G. Van Albada, B. Van Leer, and W. Roberts, "A comparative study of computational methods in cosmic gas dynamics," in *Upwind and High-Resolution Schemes*, pp. 95–103, Springer, 1997.

[42] C. K. Law, *Combustion physics*. Cambridge university press, 2010.